Experimental and numerical investigations of monopile ringing in irregular finite-depth water waves

Erin E. Bachynski[a,b,*], Trygve Kristiansen[a], Maxime Thys[b]

[a] *NTNU, Department of Marine Technology, 7491 Trondheim, Norway*
[b] *SINTEF Ocean (formerly MARINTEK), 7450 Trondheim, Norway*

Abstract

In storm conditions, nonlinear wave loads on monopile offshore wind turbines can induce resonant ringing-type responses. Efficient, validated methods which capture such events in irregular waves in intermediate or shallow water depth conditions are needed for design. Dedicated experiments and numerical studies were performed toward this goal. The extensive experimental campaign at 1:48 scale was carried out for Statoil related to the development of the Dudgeon wind farm, and included both a rigid model and a flexible, pitching-type, single degree-of-freedom model. Twenty 3-hour duration realizations for 4 sea states and 2 water depths were tested for each model. A high level of repeatability in ringing events was observed. Uncertainties in the experimental results were critically examined. The stochastic variation in the 3-hour maximum bending moment at the sea bed was significantly larger than the random variation in repetition tests, and highlighted the need for a good statistical basis in design. Numerical simulations using a beam element model with a modified Morison wave load model and 2nd order wave kinematics gave reasonable prediction of the ringing response of the flexible model, and of the measured excitation forces on the rigid model in the absence of slamming. The numerical model was also used to investigate the sensitivity of the responses with respect to damping and natural period. A simple single degree-of-freedom model was shown to behave similarly to a fully flexible model when considering changes in natural frequency and damping.

Keywords: ringing; higher order wave loads, hydrodynamic model testing; monopile; offshore wind turbine

1. Introduction

The typical lowest resonance period of large-diameter monopile support structures for offshore wind turbines (OWTs) is 3-5 seconds, which can coincide with the second, third and fourth excitation frequencies of ocean waves in representative storm conditions. Nonlinear high-frequency wave loads can therefore lead to springing- and ringing-type responses. Here, we apply Faltinsen's definition of ringing: "transient structural deflections at frequencies substantially higher than the incident wave frequencies" [1]. Ringing is thus characterized as a transient event, generally following a high, steep wave, while "springing" is characterized as a steady-state response to sum-frequency wave effects.

There is a significant body of research on ringing and springing loads and responses in deep water wave conditions, particularly related to the construction of tension leg platforms and gravity-based structures for oil and gas in the

*Corresponding author
Email address: erin.bachynski@ntnu.no (Erin E. Bachynski)

1990s. Several theoretical models were developed to describe the nonlinear wave loads which lead to ringing [1–5], and experimental validation was carried out considering both fixed and moving cylinders [6, 7].

In the hydrodynamically intermediate water depths (15-50m) which are relevant for monopile OWTs, the magnitude of the nonlinear wave loads is higher than in deep water. Load effects related to steep and breaking waves on a parked turbine may be critical for ultimate limit state (ULS) design, necessitating a better understanding of the load mechanisms and structural responses, as well as improved numerical modeling. The present work describes an experimental and numerical study of ringing of a monopile OWT in intermediate water wave conditions, accounting for natural stochastic variations in the ocean environment. One strength of the present study is the appreciable number of tests: 473 three-hour duration irregular sea states were tested experimentally.

Recently, several experimental studies have been carried out to investigate ULS wave effects on monopile wind turbines, as summarized in Table 1, including the present tests at 1:48 scale with a 6.9 m (full scale) diameter model. The objectives of the experimental campaigns vary somewhat, as do the applied scales and waves.

Table 1: Selected experimental studies of wave effects on monopiles. * indicates that the scale was not explicitly given by the authors, and is expressed here based on a full-size diameter 6.9 m. Wave conditions are classified as DBr: deterministic (focused) breaking waves; R: regular; I: irregular, LC: long-crested, SC: short-crested. Irregular wave conditions are further classified as FLS (fatigue, non-steep) and ULS (steep).

	Facility	scale	water depth (m)	model	waves
Wienke & Oumeraci, 2005 [8]	FZK	1:9.8*	39.2-44.1*	rigid	DBr
de Vos et al., 2007 [9]	Aalborg University	1:57.5*	20.1-28.7*	rigid	R, ULS I, LC
Zang et al., 2010 [10]	DHI	1:27.6*	13.9	rigid	DBr
de Ridder et al., 2011 [11]	MARIN	1:30	30	flexible	R, DBr, FLS I, LC
Nielsen et al., 2012 [12]	DHI	1:36.6	16.6-20.1	rigid	ULS I, SC
Nielsen et al., 2012 [12]	DHI	1:80	20.8-40.8	rigid/flexible	ULS I, SC
Present work	NTNU/SINTEF Ocean	1:48	19-27	rigid/flexible	ULS I, LC

Wienke and Oumeraci carried out extensive tests with deterministic (focused) breaking waves in order to develop a semi-empirical formulation of breaking wave forces [8]. These tests were carried out with a relatively large scale and depth, and considered only plunging breaking waves. As such, these tests are useful for examining short-duration slamming loads, but do not consider excitation of the lowest global mode of the monopile.

Tests at Aalborg carried out by de Vos et al. examined run-up along the monopile in order to address design concerns related to the placement of access platforms [9]. Although de Vos et al. did not measure loads on the structure, the experimental setup was similar to the present work in terms of scale and tank length. Second order irregular wave kinematics were used to develop run-up prediction formulae. One key difference in the experimental setup is related to the tank bottom: while de Vos et al. applied a ramp (1:100 slope), the waves in the present test were generated at the same depth as the monopile model.

Zang et al. suggested "re-visiting" the ringing phenomenon - known from oil and gas installations in deeper water - in the context of offshore wind turbine foundations in 2010 [10]. Through a limited number of experiments

with focused and inverse focused waves, they proposed to examine the harmonic components of the forcing. While the study was not conclusive, the formulation of the problem in terms of ringing was important, and they observed the importance of second order parasitic waves.

More extensive testing was carried out at MARIN [11]. A 1:30 flexible model was constructed to represent the mass, stiffness, and first two modes of a 6MW wind turbine with 6 m diameter at the waterline (full scale). The focus of the study was on breaking wave impacts, and an extreme case (focused breaking at the monopile) was shown to excite the first three modes of the model and to lead to accelerations at the nacelle of up to 8.9 m/s^2. Ringing-type responses in irregular wave conditions were also seen to excite the first and second modes of the tower, but no statistical analysis of these observations was shown. The tests at MARIN were carried out with a flat tank bottom.

Researchers in Denmark (DHI/DTU) have also carried out wave tank testing of flexible monopile support structures [12–15]. These tests were carried out in a wave tank with a sloped bottom (1:25) and included regular waves, irregular waves, and focused breaking waves. Short-crested (spread) seas were included in the tests. Significant vibrational responses were observed in steep and in breaking waves. Although the excitation was not distinctly identified as ringing, the results suggested that responses due to steep waves could be significant in short-crested seas (as well as in long-crested seas).

While previous experimental campaigns for monopile wind turbine support structures focused heavily on deterministic breaking waves, or on a limited number of events in irregular wave realizations, the present work, which was carried out for Statoil related to the development of the Dudgeon wind farm, makes use of a highly automated test setup such that extensive quantities of data, including numerous repetition tests, have been collected. This improved statistical basis gives new insights in the distribution of maximum loads, both for a rigid and a flexible (single-mode) structure.

In addition to experimental campaigns, numerical studies of monopile foundations have also been carried out. In order to model the complex flow in the tests at DHI/DTU, two approaches were considered: 1) a fully nonlinear Navier-Stokes volume of fluid approach with loads calculated from pressure integration and 2) Morison's equation with wave kinematics computed from a fully nonlinear 2D potential flow model of the undisturbed wave field [12, 16, 17]. Both nonlinear solvers are found to work approximately equally well in general, although the Navier-Stokes solver was found to work better for near-breaking waves. Still, both of these methods are relatively computationally expensive and difficult to apply in the ULS design of monopile wind turbines. Since the present experiments employed a flat bottom (no ramp) wave tank, it was decided to estimate the wave kinematics by means of theoretical second order reconstruction. The applicability of a modified Morison's equation with second order wave kinematics for computing the long-term statistical maximum loads is evaluated in the present work.

The modified Morison's equation has advantages in terms of simplicity, but there are inherent limitations. Other methods of accounting for spatial gradients in the undisturbed wave potential have been proposed (i.e. [5]), but neither these nor the present approach can account for local free-surface diffraction effects. Furthermore, the present work uses the linearized measured wave elevation as input to the numerical model; the ability of the numerical model to recreate the statistical wave process in the absence of measured waves (as would be typical in design) is not considered.

The experimental setup (including an error analysis) is presented in Section 2, while the numerical model is described in Section 3. Results from the experimental and numerical campaigns are presented and discussed in Section 4. The results include time series of selected events, validations of the numerical model, and an analysis of the variation and extreme values of the maximum loads and responses. Furthermore, in order to verify that the experimental findings are relevant for real structures and to extend the applicability of the observed patterns, numerical sensitivity studies were carried out where the responses of a more realistic fully-flexible model were compared to those of the single degree-of-freedom model. Variations in the damping (structural and hydrodynamic) and in the natural frequency were examined.

2. Experimental Setup

The 1:48 scale experiments were carried out in a medium size wave tank at NTNU/SINTEF Ocean (formerly MARINTEK) in Trondheim. The tank length is 28m, the tank breadth is 2.5m and the maximum water depth is 1m. For the present tests, the tank was equipped with a piston-type wavemaker. The experimental set-up is illustrated schematically in Figure 1 and selected video snapshots are shown in Figure 2.

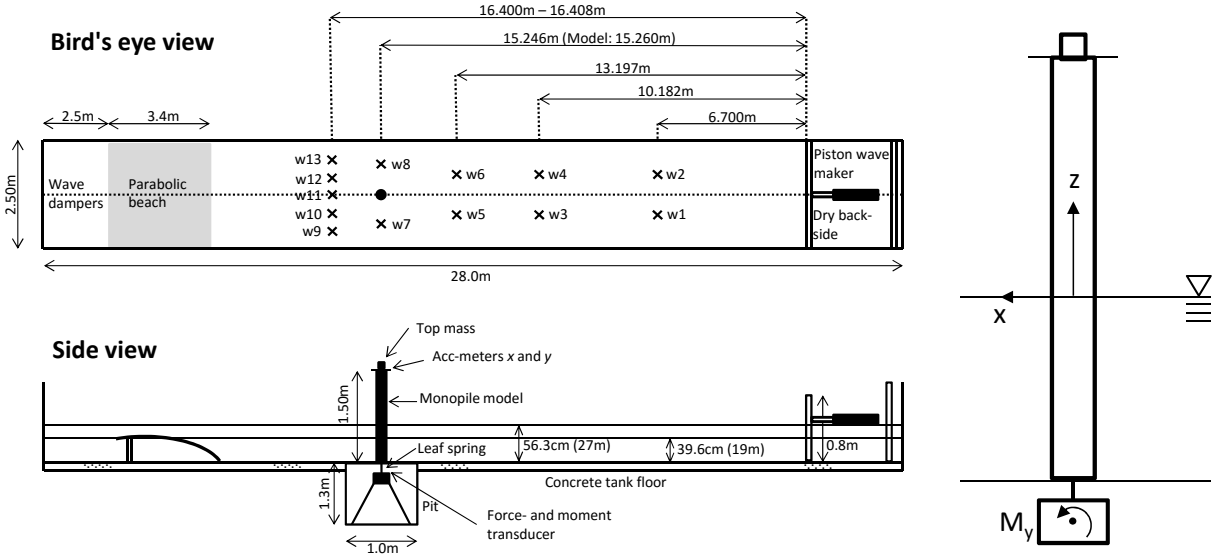

Figure 1: Model test set-up and coordinate systems of the present ringing experiments.

2.1. Model and Instrumentation

The particulars of the model are provided in Table 2. The model was constructed by a uniform aluminium pipe with diameter $D = 0.144$ m (6.9 m full scale) and wall thickness 6mm, a flange at the upper end to support top mass and accelerometers, and a bottom piece at the lower end to fix it to the dynamometer. In the flexible model tests, the model was connected to the force/moment transducer via a leaf spring made by a 5 mm $\times$ 50 mm $\times$ 50 mm aluminium plate welded to two end pieces (see Fig. 3). The aluminum pipe was relatively rigid, such that the leaf spring provided most of the flexibility and the model had a single pitching-type mode of motion. A top mass was included to mimic the weight of the wind turbine rotor and to achieve the desired natural period. Since

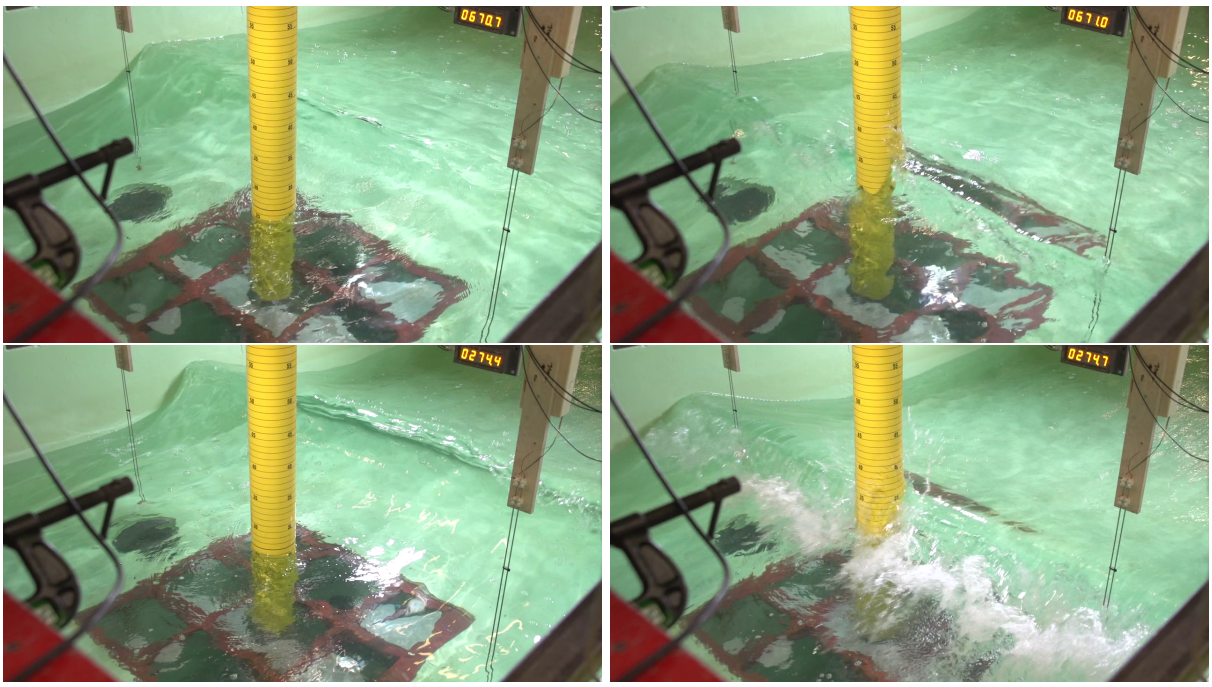

Figure 2: Snapshots from the rear view video. The time in the display is model scale. Upper: non-breaking event. Bottom: severe breaking wave event. Left: a time instant just prior to the event. Right: the time instant where the wave crest aligns with the model. Time-series of measured waves and mudline overturning moment from the two events are presented in Figure 6.

the maximum height of the model was reduced compared to a full scale wind turbine, the rotor mass was somewhat increased. The natural period in dry condition was approximately 3.7 s (0.53 s or 1.87 Hz model scale).

The model was wet inside, but filled with light-weight porous stuffing in the wetted part to avoid internal sloshing, whose lowest natural periods coincided quite closely with the natural period of the flexible model. Decay tests were performed at 27m water depth without the stuffing, showing that the internal sloshing affected the motions to a limited extent if the stuffing was not used.

In the rigid model tests, the leaf spring was replaced by a cross-bar stiffener, and the top mass was removed. The natural frequency was then approximately 23 Hz model scale (or 3.3 Hz full scale).

A transparent acrylic glass plate was used to cover the pit (see Figure 2), and care was taken to seal the area where the leaf spring or cross-bar stiffener penetrated the acrylic glass as much as possible to suppress unwanted water motion while still avoiding contact between the model and the acrylic glass plate. The distance between the bottom of the model and the acrylic glass was approximately 3mm, sufficient to avoid contact during the most extreme ringing events.

In reality, monopile structures are flexible with a range of structural modes. The simple single mode model was chosen to reduce the complexity in order to provide benchmark data with as few uncertainties as possible for the numerical work. The single mode model seeks to match the dominant aspects of the first structural mode; the natural period and a representative damping level in the range 0.5 - 2 %.

We acknowledge two main discrepancies between the present, single-mode model and a realistic elastic structure. The first is that the majority of the motion in reality occurs in the top half of the structure, and the motions in the wet part are modest. The pitching motion of the single mode model includes significantly more motion in the

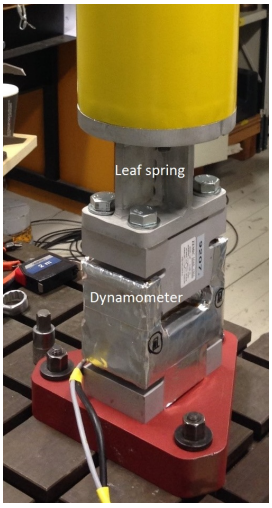

Figure 3: Force and moment transducer and leaf spring for the flexible model.

wetted part, which causes more wave radiation and viscous damping than a full scale wind turbine. The wave radiation is a dominant part of the total damping in the present tests (see Section 2.2). The second discrepancy is that the higher modes are not represented, and these may account for a non-negligible part of the maximum overturning moment near the base line, especially in wave breaking, or slamming events. In order to examine the effect of the simplified single-mode model on the interpretation of the results, some sensitivity studies were also carried out with a numerical fully-flexible model and compared to results with a numerical single-mode model (see Section 4.3).

Table 2: Model particulars. Top mass includes top flange and accelerometers. Note that the dry resonance period also includes flexibility in the dynamometer.

	Model scale (Exp.)	Full scale (Num.)
Model height	1.5 m	72 m
Diameter	144 mm	6.9 m
Wall thickness	6 mm	0.288 m
Pipe weight	11 kg	1215 metric tons
Top mass	4.07 kg	409 metric tons
Spring stiffness	2944 Nm/rad	$1.56\text{x}10^7$ kNm/rad
Pitch inertia	18.6 kgm^2	$4.73\text{x}10^6$ tonnes-m^2
Resonance period, dry	0.53 s	3.7 s

The instrumentation included a force/moment dynamometer located in the pit just below the tank floor, two accelerometers located at the top of the model (in the horizontal $x-$ and y directions, along-wave and across-wave, respectively), 13 conductance-type wave gauges, two cameras (front and rear-side views), water temperature sensor, and a position-meter to measure the piston type wave flap motion.

2.2. Decay tests

In order to characterize the model, decay tests were carried out by pulling the top of the model and releasing. Results from decay tests in the dry tank (no water), and 19m and 27m water depths are provided in Figure 4. The maximum amplitude of motion is similar to that seen during ringing events in irregular waves. Time-series of the mudline moment are shown on the left hand side. The lower plots, which all use the same time-window, show that the damping increased with water depth. This is mainly due to wave radiation damping. The critical damping ratio, ζ, obtained by standard logarithmic decay analysis, is shown on the right side of Fig. 4. Linear curve fits to the data are included, where the solid and dashed curves correspond to the peaks and troughs of the decay time-series, respectively. In the 27m water depth case, repetition tests were performed, showing some scatter, but the variation among repetition tests is significantly smaller than the difference in damping due to changes in water depth.

The nonzero slope of the linear fit for ζ shows that quadratic damping was present in the tests, and its magnitude was similar in all three cases. The origin of the quadratic damping is hypothesized to be related to welds in the leaf spring, because the same quadratic damping could be observed with and without the plexiglass plate and in both wet and dry conditions. There was no evidence of quadratic hydrodynamic damping due to flow separation. This is as expected; the amplitudes of motion in the decay tests (in still water) were small such that the Keulegan-Carpenter number was small, $KC \lesssim 1.3$. Attached boundary layer flow provides non-negligible, but non-dominant linear damping, as shown by [18]. Wave radiation damping was the dominant contributor to linear damping according to our estimates. The wave radiation damping was estimated by integrating panel pressures in WAMIT (see Section 3.2), while the contribution from boundary layer flow was found from the 2-D quadratic damping coefficient [18]:

$$C_D^F = 4\pi\sqrt{\frac{\pi}{ReKC}}, \tag{1}$$

where Re is the Reynolds' number. Since $C_D^F \propto \frac{1}{U}$ (where U is the characteristic velocity), a linear 2-D coefficient can be found and integrated along the pitching monopile. The total measured damping is larger than the estimated contributions from structural, wave radiation, and viscous damping; some additional unknown effects (such as the gap between the bottom of the model and the tank floor, or the accelerometer cables) may also play a role.

Table 3: Estimated damping during decay tests, expressed as % critical damping.

	19 m	27 m
Structural (dry decay)	0.28	0.26
Wave radiation (WAMIT)	0.41	0.98
Attached boundary layer flow	0.01	0.03
Total (wet decay)	0.83	1.30

The waves radiated by the model were reflected back from the wave-maker, as exemplified in the long time series of decay at 27 m water depth in Fig. 4. Approximately 70s after the model was released, the model was re-excited by its own radiated waves, which agrees well with theoretical time to return (69 seconds). The amplitude of the bending moment after re-reflection is approximately 6-7% of the bending moment at the instant of release. This

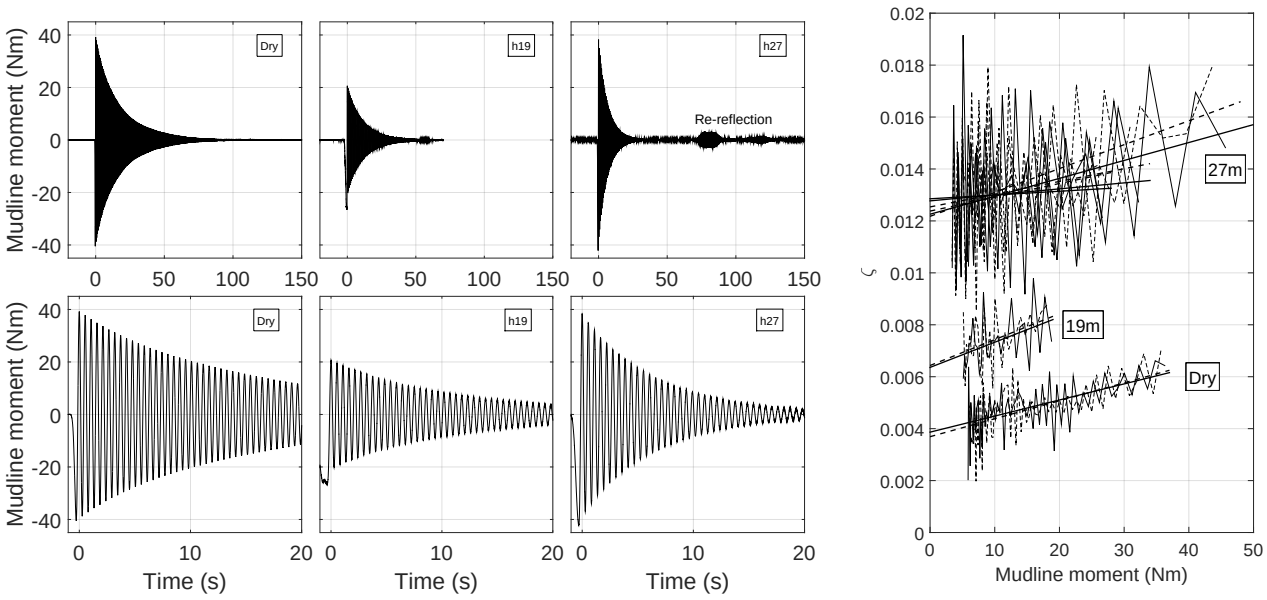

Figure 4: Decay test results (model scale). Left: Time-series from tests in no water, 19m and 27m water depths. Right: Corresponding logarithmic decay analysis showing critical damping ratio ζ. Wave radiation damping is a dominant part of the damping.

corresponds well with the fact that the monopile covers about 6% of the tank width, which is a measure of the model's ability to absorb the total returning wave energy. We must expect that this self-excitation mechanism has been present during all the irregular wave tests, representing an error source in our experiments, further discussed in Section 2.5.

2.3. Test matrix

Two water depths were chosen for the study: 19m and 27m. For the Dudgeon field, the first is a representative water depth in normal conditions, while the second is a storm surge condition. There are clear finite or shallow water depth effects, particularly at the 19m depth. For this water depth, a significant amount of wave breaking occurred along the tank.

In total, 473 three hour duration (irregular) sea states were tested. In addition, 392 regular wave tests were conducted. The regular wave tests are not discussed in the present work, but treated in [19]. The development of an automated test procedure, by programming the wave machine signal and data recording system, enabled the extensive number of realizations. The automated test procedure had two main benefits. One was that time usage of the test facility was maximized; the tests were run day-and-night, as well as week-ends, with minimal manual labour. The other was that the quality of the test results was enhanced due to the fact that the number of human errors was minimized. Over 12 hours (model scale time), 20 seeds of the same sea state were generated by the wave maker; each seed lasted approximately 26 minutes (3 hours full scale, plus time for transients), with 8 minutes (model scale) pause in between each seed to allow the basin to settle. System checks were performed in between each 12-hour test.

An overview of the test matrix is provided in Table 4. There are four sea states (combinations of H_s, T_p, and γ) and two water depths which are applied to each of the two models. These sea states all represent storm conditions. The main tests are listed in the first column. Each main test consisted of 20 three hour duration realizations, or seeds, numbered 1 - 20. The next two columns refer to repetition tests. The column denoted by Rep20 indicates whether one repetition of each of the 20 seeds was conducted. The column denoted by Rep5 indicates that seed 10 was repeated 4 or 5 times. The repetition tests were important for studying the level of repeatability in the tests, which was generally found to be quite satisfactory (see also Fig. 6).

The wave conditions in Table 4 are also characterized by a representative KC and irregular Ursell number (Ur) defined by [20]. The representative KC is calculated as:

$$KC = \frac{2\pi H_s}{D} \frac{\cosh k_p h}{\sinh k_p h} \tag{2}$$

where D is the diameter, k_p is the wave number at the peak frequency, and h is the water depth. This representative KC number corresponds to a wave with amplitude H_s (a rough estimate of the expected maximum) with the velocity according to linear theory at the mean water level. In the crest, the real wave particle velocities may be higher.

The irregular Ursell number is computed as:

$$\mathrm{Ur} = \frac{k_p H_s}{2(k_p h)^2}. \tag{3}$$

and is seen to remain below the typical validity limit for second order waves ($Ur = 0.33$).

2.4. Wave generation and wave spectra

The waves were generated by a piston-type wave maker. The space behind the piston paddle was kept dry by sealing the intersection of the paddle and steel plates on the tank wall with Teflon inserts and an applied overpressure of 1 bar. Linear wave maker theory was applied, so parasitic second order waves were present. Ideally, a second order correction to the wave maker theory should be implemented, for instance as described in [21]. The parasitic waves represent a source of error in these tests.

Examples of measured wave spectra from wave calibration tests for all eight sea state/depth combinations from Table 4 are provided in Figure 5. The thin curves represent the specified spectra, while the measured spectra at the model centerline position are represented by the thick curves. Both the amplitude and phase of the Fourier components were random numbers drawn from Rayleigh and uniform distributions, respectively, according to best practice [22]. The peak frequency $1/T_p$ (as specified) is indicated by the solid vertical curve in each sub-plot. The dashed curves labeled with numbers 1 - 4 show multiples of the natural period 3.8 s (which corresponds to the first structural natural frequency) to illustrate which wave harmonics are important. For instance, the fourth harmonic of waves around 15.2 s is of importance in the cases with $T_p = 13.2$ s, but not in the other cases.

In the 27 m water depth cases, the whole spectra are quite well reconstructed, whereas in the 19 m water depth cases, it is noticeable that wave energy is lost, in particular in the range $1/T_p \lesssim f \lesssim 2/T_p$. This is due to significant wave breaking along the tank under and after large wavemaker motions. No attempt was made to remedy this by boosting the wave maker motion, since more massive wave breaking would then occur. The distribution of wave energy depends on the water depth for these depth-to-wave length ratios (especially at 19 m water depth), and

Table 4: Test matrix. Regular and irregular wave tests. The main tests are listed in the first column. Each main test consisted of 20 three hour duration realizations, or seeds, numbered 1 - 20. The next two columns refer to repetition tests. The column denoted by Rep20 indicates whether one repetition of each of the 20 seeds was conducted. The column denoted by Rep5 indicates that seed 10 was repeated 4 or 5 times. γ is calculated as given in DNV RP-C205, except for the broad-band spectrum: $T_p = 10$s and $\gamma = 1$.

Model	Water depth	Main	Rep20	Rep5	H_s	T_p	γ	KC	Ur
Flexible	19m	20	20		6.15	10	3.04	7.24	0.16
		20			6.15	10	1	7.24	0.16
		20		5	6.7	11.5	1.9	8.76	0.21
		20		5	6.8	13.2	1	9.94	0.25
	27m	20	20	4	6.15	10	3.04	6.46	0.09
		20			6.15	10	1	6.46	0.09
		20	20	4	6.7	11.5	1.9	7.69	0.12
		20	20	4	6.8	13.2	1	8.63	0.14
Rigid	19m	20		5	6.15	10	3.04	7.24	0.16
		20			6.15	10	1	7.24	0.16
		20	20	5	6.7	11.5	1.9	8.76	0.21
		20		5	6.8	13.2	1	9.94	0.25
	27m	20			6.15	10	3.04	6.46	0.09
		20			6.15	10	1	6.46	0.09
		20	20	4	6.7	11.5	1.9	7.69	0.12
		20			6.8	13.2	1	8.63	0.14

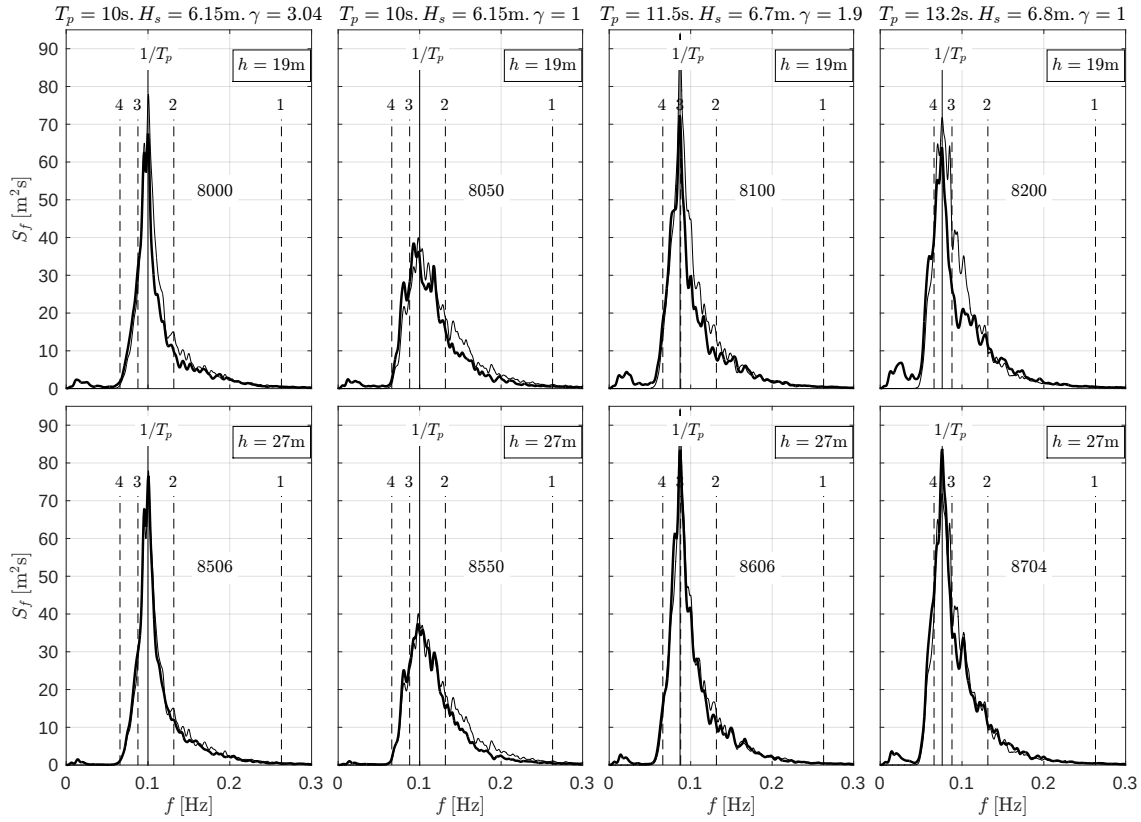

Figure 5: Examples of irregular wave spectra; seed 10 of each of the eight combinations of sea state and water depth. Measured (thick curves) versus specified (thin curves). The axes are the same for each of the plots. Upper row: $h = 19$m. Lower row: $h = 27$m. At 19m water depth, significant energy is lost for wave frequencies $1/T_p \lesssim f \lesssim 2/T_p$ due to wave breaking along the tank.

the TMA spectrum could be more realistic than the specified JONSWAP spectrum [23]. Implementation of the TMA spectrum was not attempted here, but could be investigated in further studies. The high frequency tail of the measured waves is quite well reconstructed in the experiments at both water depths, except for the broad-band spectra ($T_p = 10$s and $\gamma = 1$). The low-frequency energy seen in the measured spectra is related to set-down effects. The set-down (or rise-up) is not expected to provide significant forcing on its own, but can modify the moment arm of higher-frequency loads for individual wave events.

2.5. Assessment of Experimental Error

Experimental error and uncertainty are inherently present in model tests. Although it is not possible to quantify all error effects, it is important to consider finite tank effects, measurement accuracy, and repeatability. Table 5 summarizes the error sources which were examined, and their expected impact on the results.

The finite extent of a wave tank is of general concern because wave energy is not transported away to infinity. Wave reflections and blockage effects should therefore be considered. In the present test, the ratio between the model diameter and tank breadth was small enough that blockage effects are negligible. This can be seen by considering the potential flow solution of a 2D circular cylinder in infinite fluid, which causes a disturbance of the flow $\propto (a/r)^2$, where a is the cylinder radius and r is the radial distance from the cylinder center. Here, $a/r = 1/17$ at the tank

Table 5: Brief summary of experimental error sources. Velocities are given in full scale.

Error source	Quantification	Comment
Blockage / tank breadth to model diameter ratio	1:17	Negligible blockage (< 0.3 %)
Side wall reflections		Reflection of high modes
Beach reflections	up to 10 %	Significant for regular wave tests
Self-excitation/ wave maker reflections	Appr. 6 %	Small effect on maxima
Seiching	0.08 m/s	Insignificant
Pumps	0.07 m/s	Insignificant
Water depth variation /Refraction	< 1 %	Waves were symmetric
Shear/moment dynamometer	1 %	Static tests
Wave gauges	2 % + 2 %/deg C	Corrected for temperature

wall. The effects of reflections (of diffracted waves) from the side walls are less clear. The first order diffraction is negligible due to the long wave regime for the majority of the wave frequency content, but second and higher order diffraction may be significant, and may be affected by reflections from the side walls.

Attempts were made to limit reflections from the beach. The beach was of parabolic shape, consisting of 4 % perforated plates fixed to a rigid framework which was fastened to the tank floor. A thorough reflection analysis was not performed, but a reflection level of about 10 % for $T > 12.5$s, and less than 3 % for $T \leq 12.5$ was estimated based on regular wave tests.

Self-excitation - waves generated by the model and reflected back from the wave maker - had a measurable effect. This was illustrated by the decay test at 27 m water depth presented in Figure 4. It is not easy to state exactly how much impact this had on the results. If we consider the maximum overturning moment at mudline during a ringing event, the response depends on the ringing wave load itself and the state of the system as the wave enters, i.e. the underlying springing response. In terms of magnitude, the maximum bending moments after the major ringing events are typically about three times higher than those caused by the underlying springing motion. Based on the model's ability to absorb approximately 6 % of the re-reflected energy, and that the reflected energy is primarily due to springing events, re-reflection could account for about 2 % of the maximum response magnitude. Despite the limited magnitude of the loads due to re-reflection, their effect on the phasing of the underlying springing motion may nonetheless have a greater impact on the ringing responses (see Section 4.1). For tests with a more realistic mode shape, the self-excitation would be less pronounced: the motion of the wet part would be significantly smaller, with consequently less radiated waves.

Seiching corresponds to longitudinal standing waves in the tank. The periods of the two first modes are $2L/\sqrt{gh}$ and $L/\sqrt{gh}$, where L is the length of the tank. This means 56s - 160s (full scale). A slowly oscillating current is associated with the seiching motion. With the observed seiching wave amplitudes, these corresponded to current amplitude of up to 0.08 m/s (full scale) at the model position. Compared to typical wave particle velocities in extreme events exceeding 3-4 m/s, this is small. An additional, unrelated current was also present due to leakage behind the wavemaker piston flap and corresponding pumping of water. The volume flux corresponded to

approximately 1 mm/s model scale, averaged over the tank cross-sectional area. This corresponds to 0.07 m/s full scale, which is expected to give similarly small effects.

Shallow water waves are sensitive to transverse variations in the water depth due to refraction. In order to limit refraction effects, the tank floor was levelled prior to the experiments. The variation in water depth was less than 1 mm in the transverse direction throughout the tank, and 1-2 mm in the longitudinal direction in the last 2/3 of the tank (the 1/3 closest to the wave maker was approximately 3-4 mm deeper). No evident signs of refraction were observed visually or by the measurements (wave gauge pairs).

A significant effort was made in keeping measurement errors low. The shear/moment dynamometer was calibrated before the tests, and checked regularly during and after testing. Static tests over the course of the experimental campaign showed that the variability in base shear and overturning moment measurements were within 1%. Conductance-type wave gauges were used, and were calibrated to absolute variability (maximum deviation between two wave gauges) within 2% for small-amplitude linear waves before the tests. The agreement for larger wave amplitudes is significantly better. Due to temperature variations in the tank, corrections to the wave gauge measurements were applied in post-processing of the data by using the mean measured temperature over each sea state.

2.6. Repeatability

Finally, repeatability will be considered in greater detail. Regarding the wave maker motion, each wave was run at least three times: wave calibration test, rigid model test and flexible model test. The absolute deviation of the wave maker motion between tests was less than 0.4 %.

Time-series from one major ringing event and one breaking wave event are provided in Fig. 6, illustrating the typical level of repeatability of the loads. The time series correspond to the video snapshots in Fig. 2. Results from the flexible model test (response) and corresponding rigid model test (load) are presented together in Fig. 6. The tests were repeated five times, meaning that results from twelve runs are presented. The deviation of the peak mudline moment is within 1-2 % in the (representative) non-breaking case, while breaking wave events are less repeatable. The deviation of the mudline moment is around 8-10 % in the breaking case. The repeatability level for the non-breaking event (top) is representative of the major part of the tests.

With the flexible model, there are five combinations of wave condition and water depth where seed 10 was repeated 6 times in total. The variation in the maximum wave elevation, shear force, and mudline moment is summarized in Table 6. The coefficient of variation is computed as σ/μ, where σ is the standard deviation of the 6 maxima and μ is the mean of the 6 maxima.

3. Numerical model

A numerical model of the experimental setup at full scale was created in SINTEF Ocean's nonlinear beam finite element code RIFLEX.

3.1. Structural model

The RIFLEX model included beam elements which were used to represent the dynamometer, the single element leaf spring, the wet part of the monopile, and the dry part of the monopile. The internal fluid (water) was included

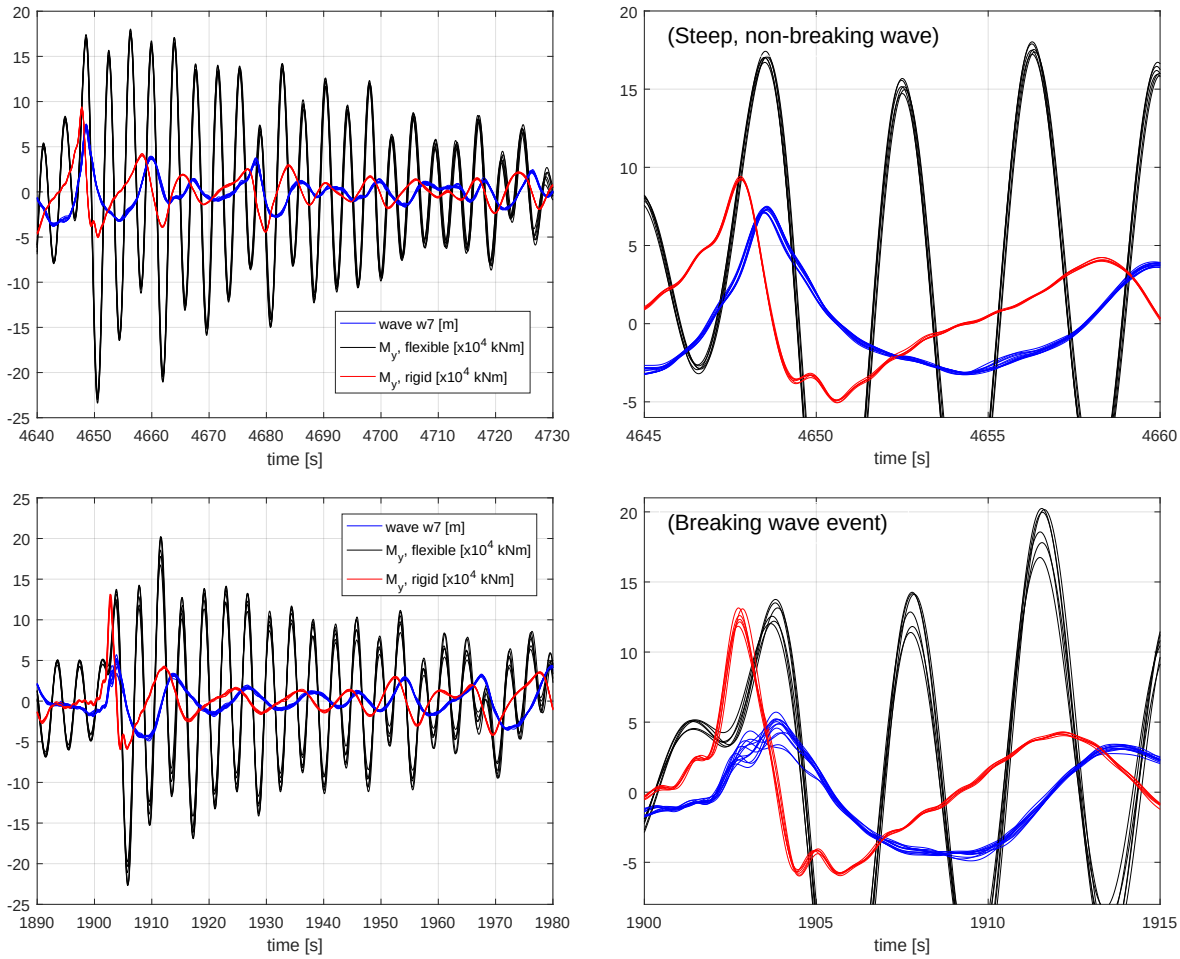

Figure 6: Illustration of typical repeatability level in the tests. $H_s = 6.7$ m, $T_p = 11.5$ s, $\gamma = 1.9$, water depth $h = 27$ m. Steep, non-breaking ringing event (top) and breaking wave event (bottom). The figures to the right are zoomed views of the left figures M_y indicates overturning moment at the dynamometer. Six tests with flexible model and six tests with rigid model are shown.

in the mass model of the wetted elements. Parameters describing the structural model and discretization are given in Table 7.

In Table 7, note that the Young's modulus for aluminum at model scale is 65 GPa, but that this corresponds to a higher stiffness at full scale. Since the computations are intended to reflect the model at "full scale," the scaled-up stiffness must be used. The coating in the experiment was paint. An additional point mass (451 tonnes) was used to represent the top mass. The flexibility in the dynamometer was represented by a flexible joint, with rotational stiffness 6.245e+06 kNm/deg.

Structural damping was applied as stiffness-proportional Rayleigh damping, determined based on the decay test of the structure in air, without top mass. The structural damping coefficient was $a_2 = 0.00125$s, which corresponds to 0.5% of the critical damping when the top mass is present.

Table 6: Coefficent of variation, flexible model tests with 6 repetitions.

Water depth (m)	H_s (m)/T_p (s)/γ	$\sigma_{\eta_{max}}/\mu_{\eta_{max}}$	$\sigma_{F_{x_{max}}}/\mu_{F_{x_{max}}}$	$\sigma_{M_{y_{max}}}/\mu_{M_{y_{max}}}$
19	6.7/11.5/1.9	0.0229	0.0439	0.0574
	6.8/13.2/1.0	0.0202	0.0128	0.0244
27	6.15/10.0/3.04	0.0221	0.0093	0.0138
	6.7/11.5/1.9	0.0135	0.0321	0.0148
	6.8/13.2/1.0	0.0127	0.0123	0.0318

Table 7: Structural model in RIFLEX.

Line	Length (m)	Number of elements	Cross-section
dynamometer	8.64	6	$D = 3$ m, $t = 0.1$ m, $E = 2100$ GPa
spring	2.4	6	2.4 m x 0.384 m, $E = 3312$ GPa
monopile (wet)	h	19 or 27	$D = 6.912$ m, $t = 0.288$ m, coating 0.044 m, $E = 3312$ GPa
monopile (dry)	$72.0 - h$	45	$D = 6.912$ m, $t = 0.288$ m, coating 0.044 m, $E = 3312$ GPa

3.2. Wave load model

The hydrodynamic loading in the numerical model is based on a modified Morison model, applied to each strip of the monopile:

$$\mathrm{d}F_h = \rho\pi\frac{D^2}{4}\mathrm{d}z a_h + \rho\pi\frac{D^2}{4}\mathrm{d}z C_a(a_h - \ddot{x}) + \frac{\rho}{2}D\mathrm{d}z C_D(u_h - \dot{x})|(u_h - \dot{x})| - \rho\sqrt{gD}D^2 C_L \mathrm{d}z\dot{x}, \tag{4}$$

where a_h and u_h are the undisturbed wave particle total acceleration (including the advective terms) and velocity, respectively. For the acceleration, we use:

$$a_h = \frac{\partial u}{\partial t} + u\frac{\partial u}{\partial x} + v\frac{\partial u}{\partial y} + w\frac{\partial u}{\partial z} \tag{5}$$

(the transverse velocity v is zero for long-crested waves). Furthermore, in Eq. 4, ρ is the density of fresh water, D is the mean diameter of a vertical strip of the monopile, C_a is the so-called mass coefficient, C_D is the quadratic drag coefficient, and C_L is a linear damping coefficient. The structural velocity is $\dot{x}$ and the structural acceleration is $\ddot{x}$. The first two terms on the right hand side are usually referred to as the inertia terms, the third as the quadratic drag, or viscous, term, and the final term is a linear damping term used to account for the wave radiation damping at the natural period. Note that only the local acceleration is included in the standard Morison's equation. We therefore refer to the presently used load model as a *modified* Morison model. Our model differs from the FNV [24] model in that the term $u\frac{\partial u}{\partial x}$ is included in the added mass term, and the third order diffraction term is omitted. Due to the relatively large motions of the single degree-of-freedom model at the waterline, the linear damping term was found to be important.

In all of the simulations with irregular waves, we have taken $C_D = 0.9$ and $C_a = 0.772$ and applied a time step $dt = 0.1$ s. Both coefficients are reasonable average values based on the KC and Reynolds numbers of steep ULS wave events [25]. More detailed estimates of C_D and C_a, depending on KC and Reynolds number for each sea state

and depth, could also be considered, but this simplified approach was found to be sufficient for investigating the higher-harmonic load components. The value of C_L varied with depth in order to mimic the radiation damping in the system. The stripwise radiation damping coefficients were computed using integration of panel pressures from the radiation potential flow solution, acquired by using WAMIT, at the natural frequency of the model. Two potential flow solutions were considered - one for surge motion, and another for pinned rotation about a point at the seabed. The two approaches gave similar results for the depth-dependent sectional linear damping coefficients (for transverse element motion). Fig. 7 compares the stripwise damping coefficients obtained by each method.

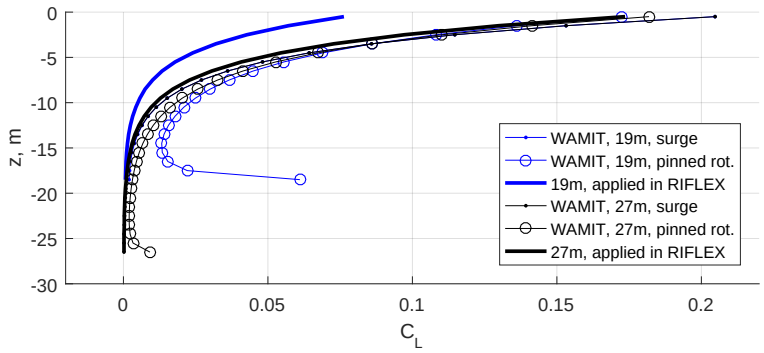

Figure 7: Linear damping coefficient C_L, as calculated in WAMIT and as applied in RIFLEX (see Eq. 4).

When combined with the structural damping coefficients from the dry decay tests, the coefficients obtained in WAMIT were found to overpredict the damping in the wet decay tests, and the sectional coefficients applied in the RIFLEX model were therefore scaled down consistently from the obtained coefficients, as shown in Fig. 7. For 19 m water depth, a factor of 0.45 was used for the surge coefficients, while for 27 m, a factor of 0.8 gave the best match. The reason for this discrepancy is not understood.

The simulations were carried out with three different wave kinematics models, as described in Table 8, in order to see the effects of the different load components. The 2nd order wave formulation follows [26]. If we consider only the terms in Eq. 4 which are related to a_h, the R0 model can be considered as a purely linear model, while the R1 model captures some 2nd order effects due to the integration of the loads up to the linear free surface. In the R1 model, the kinematics above the free surface are taken to be those of $z = 0$. The R2 model includes some 3rd and 4th order effects due to the integration of second order kinematics up to the 2nd order wave elevation. Keeping second order components in the Taylor expansion, the wave kinematics above $z = 0$ are extrapolated from the first order potential. As indicated in Fig. 5, wave loading at frequencies at twice and three times the primary wave frequencies is important due to excitation the natural frequency of the model. Due to the viscous drag term, the R0 model includes some forcing at three times the wave frequency which can excite the model. For the given conditions, however, the loads are inertia-dominated. The steepness of the wave during the zero upcrossing (associated with high horizontal wave particle accelerations) is therefore expected to be important for the structural response.

It should be noted that the present modified Morison's equation is a significant simplification of the real physical problem. First order near-field diffraction effects are not expected to be important for the present situation; the importance of 2nd and higher order diffraction (which is not modelled) is not well known. For larger oil and gas structures in deep water, ignoring the 2nd order diffraction terms is known to result in overestimation of steady-

Table 8: Load models

Model	Description
R0	1st order wave kinematics, integration to $z = 0$ (original Morison model)
R1	1st order wave kinematics, integration to undisturbed 1st order wave elevation (constant kinematics above $z = 0$)
R2	2nd order wave kinematics, integration to undisturbed 2nd order wave elevation (modified Morison model)

state springing loads [28]. The regular wave tests in the present campaign also suggest that the same overprediction occurs for the 2nd and, in particular, the 3rd harmonic for similar wave conditions and water depths [19]. The present work compares this simplified method against experimental results; more refined load models which can more correctly model the wave-structure interaction should be considered in future work.

The same linearized measured wave elevation (in the absence of the model) was given as input to RIFLEX regardless of the wave kinematics model. The linearization process attempts to remove second- and higher-order components of the wave elevation from the signal, while keeping the linear components in the tail of the spectrum. The cut-off frequency and roll-off in the applied low-pass filter depend on the wave conditions and water depth, and are iteratively chosen based on the second order reconstruction of the wave elevation. An example of the measured, linearized, and second order reconstructed wave elevation is shown in Fig. 8. In this example, the cut-off is near 0.13 Hz, which is significantly lower than the deep water recommendation $\omega = \sqrt{(2g/H_s)}$ given by [27]. The results of the response analysis are sensitive to the choice of cut-off and roll-off in the linearization.

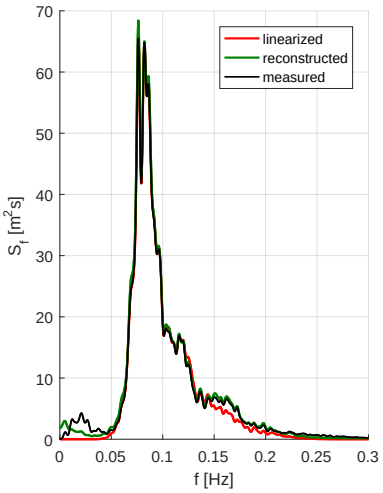

Figure 8: Measured, linearized, and reconstructed wave spectra for one realization with H_s 6.7 m, T_p 11.5 s, γ 1.9, water depth 19 m.

4. Results

As described in Table 4, experiments were carried out for 20 three-hour duration realizations of four sea states for two physical models and two water depths, corresponding to a total of 320 basic cases. Each of these cases was also simulated numerically using three models of the wave kinematics, such that 960 simulations were carried out. In this section, we present and discuss the main results. General trends and selected events are examined by means of examples of time-series comparisons of simulations and experiments in Section 4.1. The variation and distribution of maximum responses are discussed in Section 4.2. Lastly, numerical sensitivity studies related to the level of structural and hydrodynamic damping and to the natural frequency of the model are presented in Section 4.3.

4.1. Time series examples

A full 3-hour experimental realization is illustrated in Fig. 9, which includes the waiting period after the conclusion of that realization. These time series, as well as the corresponding spectra provided in Figure 10, highlight the response of the single-mode model at its natural frequency. In addition to the dynamic amplification related to ringing events, there is also a significant underlying, springing-type, response ahead of the events. The underlying motion has consequences for the maximum loads, through the phasing with the ringing load. This naturally applies to ringing of all kind of structures, but is perhaps more evident here since the underlying motion has a quite large amplitude relative to those at maximum loads. If the pitching motion of the model is a minimum (pitched towards the wave) when the load is at its maximum, the underlying motion will add to the maximum load. We refer to this as *additive* or unfavorable phasing. In the other extreme case, the phasing *non-additive*, or favorable for the structure, since it will cause the maximum response to be lower than if the model was at rest or in any other state. In the two examples provided in Figure 6, the upper is additive while the lower is non-additive.

Four selected ringing events are examined here in order to study the behavior of the model, and in order to compare the experimental and simulation results in detail. The wave elevation, shear force, and overturning moment at the dynamometer for the selected events are shown in Fig. 11-14. Results from the rigid model, which can be interpreted as the external hydrodynamic loads, and from the flexible model, including the dynamic response, are shown. When available, experimental results from repetition tests are included.

Fig. 11 exemplifies the results from 19 m water depth for a non-breaking, steep wave event. By comparing the calibrated wave elevation with the simulation results, one can clearly see that the 2nd order theory is an improvement over the first order theory in terms of the crest height and steepness. Still, the physical wave in the basin contained more nonlinearity than a 2nd order model was able to capture, as illustrated by the higher crest of the measured wave. The 2nd order (R2) model underestimates the maximum hydrodynamic force and moment acting on the rigid monopile in the given example by about 15 %. Despite the underestimation of the maximum hydrodynamic loads, the 2nd order model was able to predict the *response* of the flexible model fairly well (10 % overprediction). The R1 and R2 models both captured some of the resonant response, while - as expected - the R0 (linear wave kinematics and integration to the mean free surface) model showed primarily wave-frequency response. The R2 model captured the ringing response more accurately than the R1 model, but the springing response prior

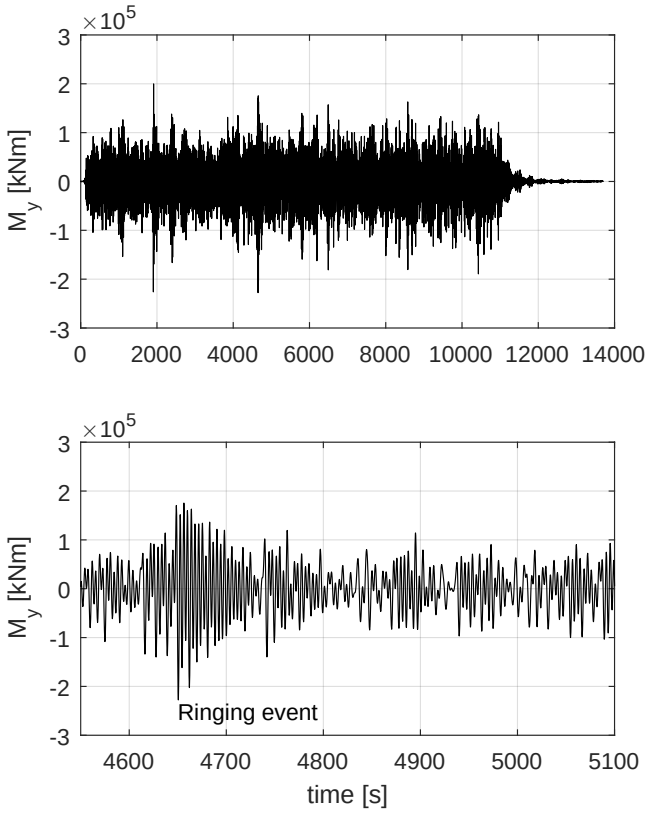

Figure 9: Examples of measured mudline overturning moment (same test as Fig. 6). Full scale values are shown. Upper: complete three-hour realization including waiting after the test. Lower: zoom-in around the non-breaking ringing event.

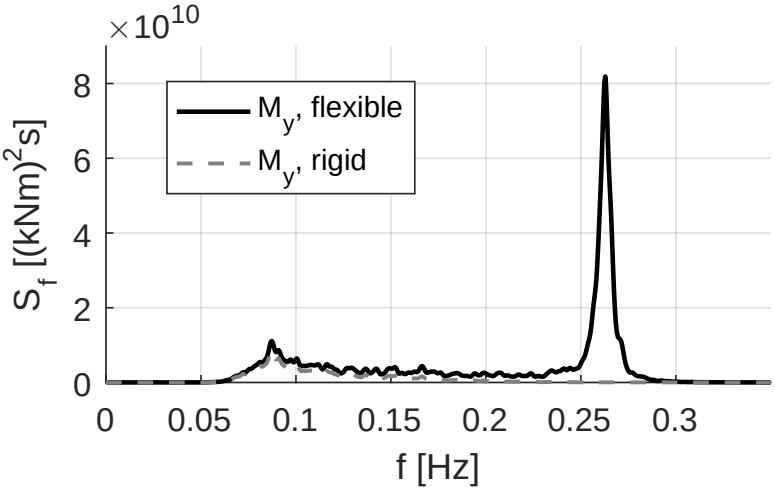

Figure 10: Power spectra of the overturning moment at the dynamometer for the rigid and flexible tests, showing the strong dynamic amplification at the natural frequency.

to the large wave passage was overpredicted by the R2 model. For the given wave condition with $T_p = 11.5$ s, the 3ω (3rd harmonic) loads are expected to have dominated the response.

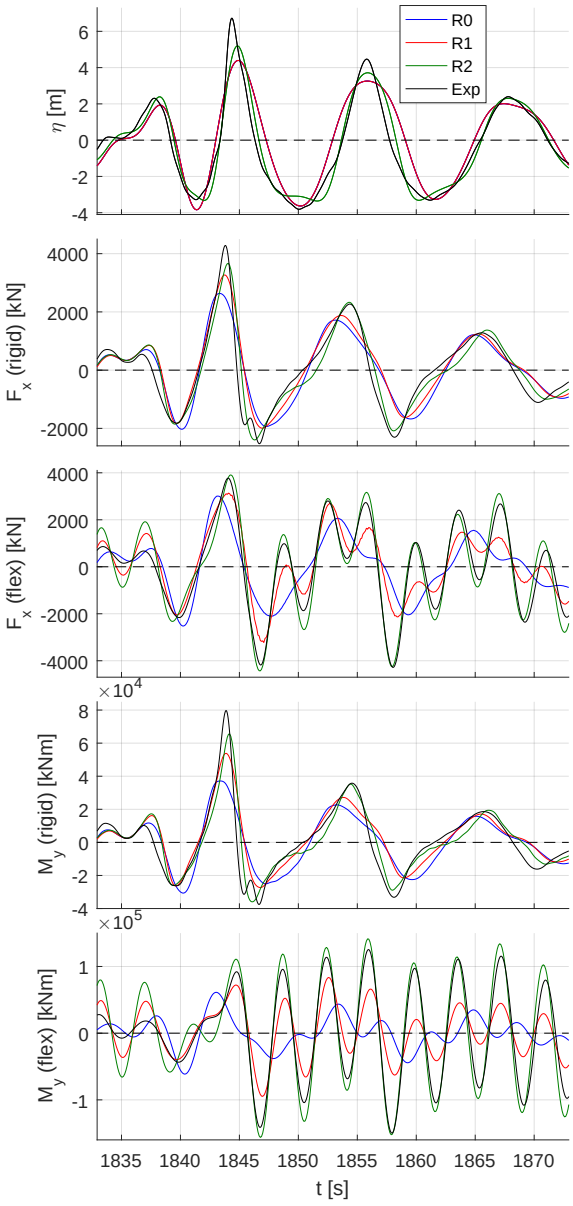

Figure 11: Time series of the calibrated wave (top), shear force (two and three) and overturning moment (four and five). Results for the rigid and flexible structure are shown in separate subplots. The time window corresponds to the largest bending moment for the flexible model from one of the experimental realizations with H_s 6.7 m, T_p 11.5 s, γ 1.9, water depth 19 m. Additive phasing. Measured results from the experiment are denoted Exp.

Fig. 12 shows an example of the same wave condition as in Fig. 11 but for 27 m water depth. Compared to the results for 19 m, the R2 model captured the maximum hydrodynamic loads on the monopile relatively well for 27 m, although the maximum wave elevation was still underpredicted. The maximum load was here slightly overpredicted by the R2 model. Good agreement between the R2 model and the experiments is seen in the maximum dynamic response. The amplitude of the springing response prior to the event was captured by the R2 and R1 models, and the phase of the springing response is in good agreement with the experiment for the cycles prior to the passage

of the large wave. A general trend is that the numerical model (R2) is in better agreement with the experiments at 27 m than at 19 m water depth. We believe that this can - to a certain extent - be explained by the fact that the 2nd order wave model is partly outside its range of applicability at 19 m (and sometimes also at 27 m) for our considered cases. Furthermore, the wave nonlinearity is expected to be more severe in 19 m than in 27 m water depth.

The limitations of the applicability of the 2nd order wave kinematics can be seen by examining the wave elevation time series R2 in Figs. 11 and 12. In the 19 m water depth (Fig. 11), a non-physical "bump" in the R2 wave elevation can be seen around 1850s, indicating that the second order theory is not valid. The same wave condition in 27 m water depth in Fig. 12 does not reveal similar "bumps".

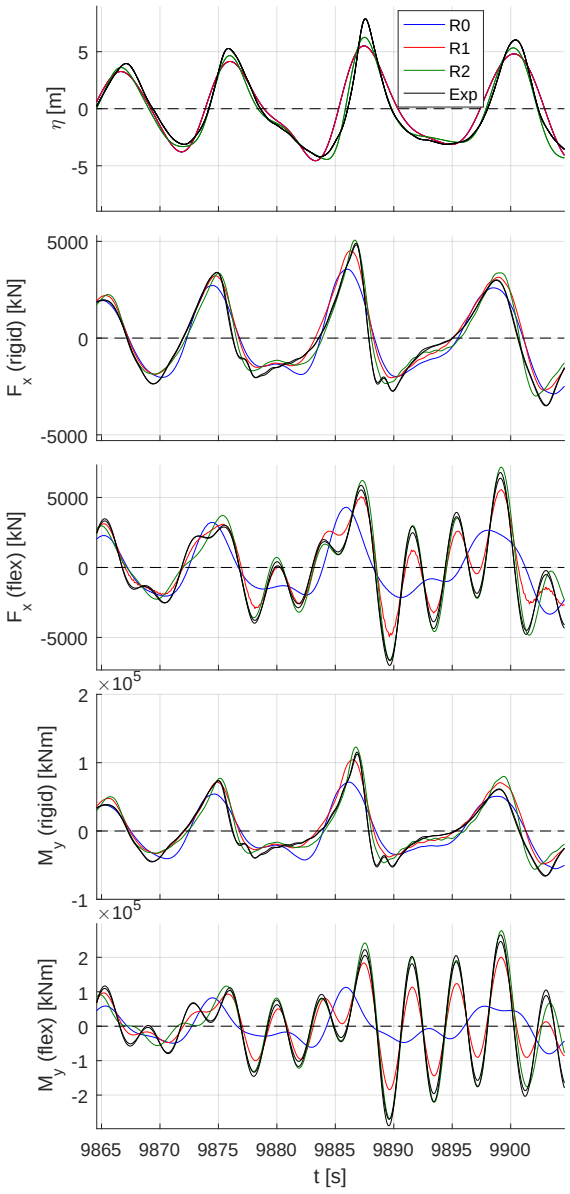

Figure 12: As in Fig. 11 for H_s 6.7 m, T_p 11.5 s, γ 1.9, water depth 27 m. Additive phasing.

The importance of the springing response on the ringing response is exemplified in Fig. 13. Comparing Figs. 12

and 13, the maximum wave elevation and hydrodynamic loads on the rigid cylinder can be seen to be similar. The numerical simulations with R2 are seen to capture the hydrodynamic loading quite well. The experimental results show, however, that the dynamic response following the steep wave in Fig. 13 was much smaller than in Fig. 12. In the event in Fig. 12, the structure was already accelerating in the same direction as the maximum hydrodynamic load at the time of the maximum hydrodynamic load (additive phasing). This can be seen in the last two subplots: at the time instant where the maximum wave-induced moment occurred, the high-frequency part of the bending moment in the flexible structure was already increasing. In Fig. 13, the springing-induced moment had already reached its maximum value and was decreasing at the time when the maximum hydrodynamic moment was applied (non-additive). The subsequent response was approximately 40 % smaller than in Fig. 12. Furthermore, the R2 numerical simulation, which didn't match the phase of the springing response in Fig. 13, is seen to underpredict the response for that particular event. The reason for the discrepancy in the underlying springing motion is not understood. Beach reflections, re-reflections, parasitic second order waves, and higher order diffraction can all contribute to differences in the springing response.

Finally, Fig. 14 shows an extreme event in 27 m water depth with slamming-type loads from a breaking wave. As shown, the measured wave-induced moment on the rigid cylinder was slightly larger than the corresponding positive bending moment of the flexible model. The subsequent negative bending moment for the flexible structure was, however, significantly higher. This case also illustrates the challenges encountered when measuring the loads on the rigid model: the experiments were designed to capture the ringing excitation from steep, non-breaking waves, but the system was not sufficiently stiff to accurately capture the high-frequency peaks in slamming-type loads: the natural frequency was 23 Hz (model scale). The results shown in the present work include a filter at 10 Hz model scale. Fig. 15 exemplifies the effects of this filter for a breaking wave event. In Fig. 14, one can also see a non-physical bump in the wave elevation at 4602 s, indicative of exceeding the limits of second order wave theory, even at 27 m, due to the steepness of this event.

To summarize, a few general observations can be made from the time series of results, such as those shown in Fig. 11-14:

1. The global hydrodynamic loads were observed to be inertia-dominated, as can be expected with the governing low KC numbers (see Table 4), and a maximum positive load occurred approximately at the part of the wave time-series with the fastest rise-time, where the horizontal acceleration (of the undisturbed wave) was largest. Locally, viscous effects may be important, especially since the estimated KC numbers do not account for nonlinearity in the wave kinematics.
2. The 2nd order wave model (R2) approximated the wave elevation of steep wave events significantly better than the first order models (R0 and R1), although the maximum crest heights in general were underpredicted compared to experiments. This is as expected, since the experimental waves contain more nonlinearity than that predicted by 2nd order wave theory.
3. There was significant dynamic amplification: the flexible model experienced larger load effects than the measured loads on the rigid model, typically about 3 times larger in non-breaking ringing-type events.
4. There was an underlying springing (steady-state) response present in both the experiments and the R1 and R2 simulations. This was observed across all of the tests. The R2 simulations tended to overestimate the

springing responses, especially in the 19 m water depth. The springing response had a noticeable effect on the maxima of the ringing response. Re-reflections (from waves generated by the flexible model) are considered to be a relevant error source in this respect, and the simplicity of the load model (which does not account for first or second order near-field diffraction) may be a reason for overestimation.

5. Ringing-type responses were seen after the passage of a large, steep wave. The maximum absolute value of the response was often in the negative direction (after the initial large positive load). The ringing response decayed slowly, "riding" on top of the first order response. The magnitude of the ringing response was typically best estimated by the R2 model, but was not consistently over- or under-estimated (see also the previous point and Section 4.2).
6. Although not shown explicitly in the selected time series results, the maximum response of the flexible model did not necessarily correspond to the maximum load on the rigid model. Slamming-type peak loads from breaking waves were generally larger than steep wave loads, but the flexible structure exhibited larger response to steep *non-breaking waves*, as the slamming loads were of very short duration compared to the structural natural period. Slamming loads may become more important if a fully-flexible model is considered [29].
7. The second order wave model was observed to be outside its range of validity for certain long and steep wave events, particularly at the 19 m water depth.

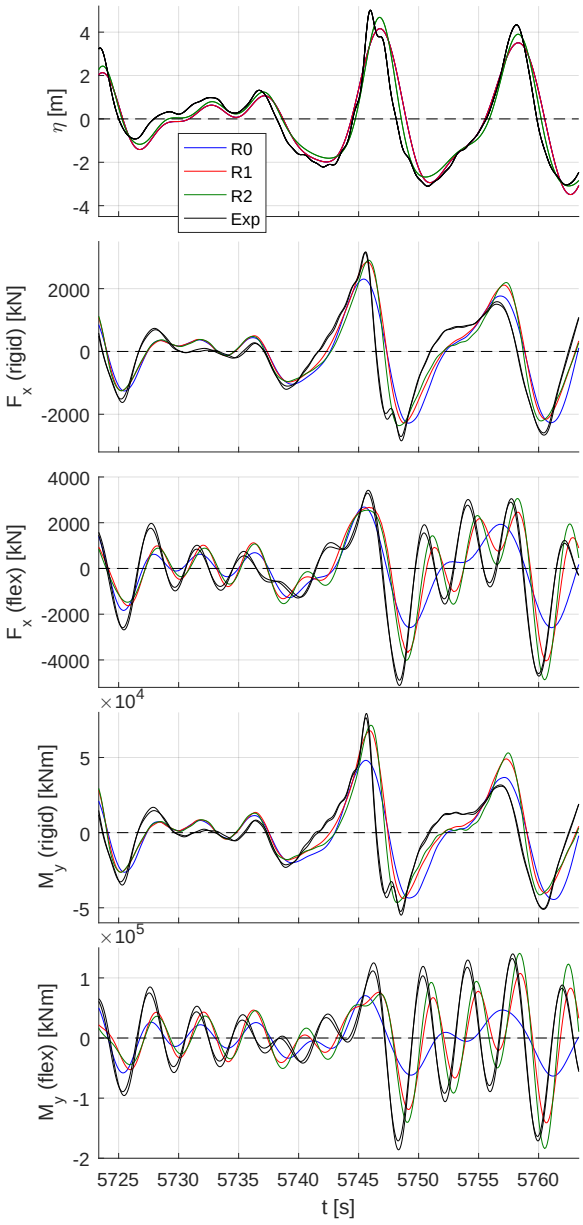

Figure 13: As in Fig. 11 for H_s 6.7 m, T_p 11.5 s, γ 1.9, water depth 27 m. Non-additive phasing.

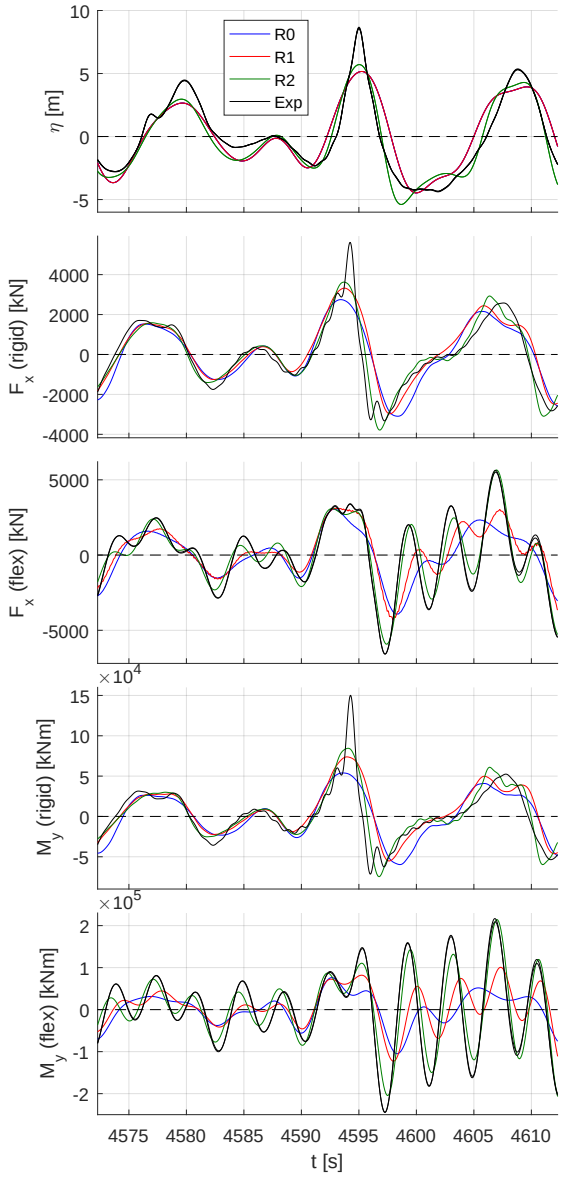

Figure 14: As in Fig. 11 for H_s 6.8 m, T_p 13.2 s, γ 1, water depth 27 m. Slamming event.

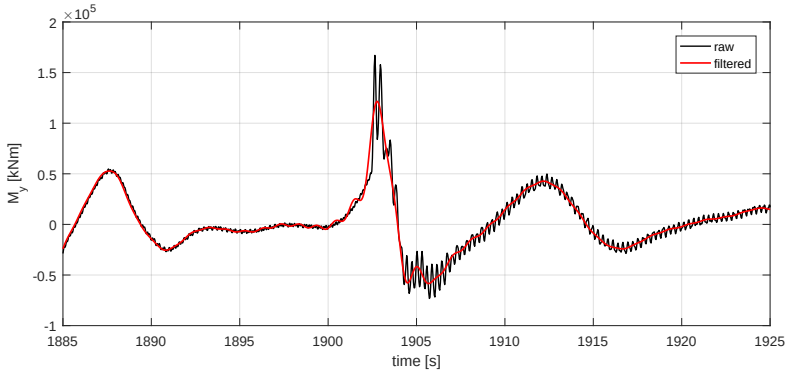

Figure 15: Raw and filtered bending moment for the rigid model, breaking wave event from Fig. 6.

4.2. Variation and distribution of maximum responses

It is interesting to examine the variability in the maximum responses from each of the 20 sea states from the experiments.

The relative variation in the maximum wave elevation, shear force, and overturning moment was calculated based on the standard deviation and the mean value of the 20 maxima, as shown in Fig. 16. Only the initial tests (no repetition tests) were considered, but all results - including slamming-type events - were included. A first observation from Fig. 16 is that the variation in the loads and responses was significantly greater than the variation in the maximum wave elevation. For the wave elevation, $\sigma/\mu \approx 0.05$, while for F_x, $\sigma/\mu \approx 0.05 - 0.15$, and for M_y, $\sigma/\mu \approx 0.07 - 0.2$. Here, μ is the mean value and σ is the standard deviation. Furthermore, the relative variation in the loads on the rigid structure was generally larger than that of the response in the flexible structure. The variation among the different seeds was significantly (2-10x) larger than that of the random variation in the maxima (shown in Table 6).

The relatively large stochastic variation (10-20 %) in the loads highlights the need for a good statistical basis in design.

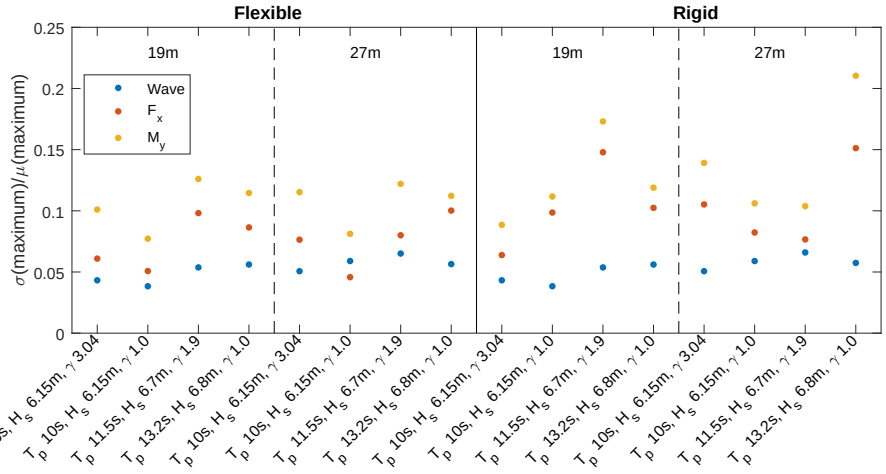

Figure 16: Variation in maximum values (standard deviation of maxima from 20 seeds divided by mean maximum value for the same 20 seeds).

The maximum responses can also be used to examine the distribution of extreme values. For each combination of sea state, water depth, and structural model, a Gumbel distribution of the measured and simulated bending moment, such as those shown in Fig. 17, was generated. Alternative extreme value distributions, such as Fréchet, were also considered, but the Gumbel distribution was found to give the best fit for the experimental data with the flexible model. First, the nine highest independent peaks in the bending moment at the mudline were extracted for each of the three-hour experimental realizations (or seeds). Corresponding peaks in the simulation results were also extracted for comparison. The simulation results typically had peaks coinciding with the experiments, such that the presented maxima also correspond to the true maxima from simulations. The largest peak from each 3-hour realization was included in the fitting (by the method of moments) of a Gumbel distribution, as exemplified in Fig. 17. For the rigid models, an additional set of results - labeled "Exp-NS" - is included. The Exp-NS results (or,

"experiment, non-slamming") indicate an attempt to remove slamming events. For the Exp-NS results, maxima which were larger than 1.2 times the median of the obtained top nine maxima (within a given 3-hour realization) were removed. This criterion was somewhat arbitrary, but seemed to reasonably identify slamming-type events based on comparison with the video for selected realizations.

The results in Fig. 17 exemplify the trends which were observed. For the flexible model, the R2 numerical model is seen to approximate the experimental results reasonably well, while the R1 model is generally non-conservative. For the rigid model, the numerical model captures non-slamming events reasonably well. In the 27 m rigid model case, it may seem that the R1 model gives a better match to the Exp-NS results. This might be explained by the fact that (large and steep) waves which in reality were breaking were still included in the input to the numerical model. Furthermore, it is interesting to note that the experimental results which do include slamming are characterized by a significantly different Gumbel distribution than the non-slamming loads. This is particularly evident at 19 m water depth (top right plot). There is higher uncertainty in the measurement of the slamming loads due to the frequency of data capture and possible dynamic amplification (of the rigid model), so the "slamming" results should be interpreted with caution. The slope of the Gumbel distribution for the maximum bending moment in the flexible model is slightly underpredicted for the 19 m depth, and slightly overpredicted for 27 m.

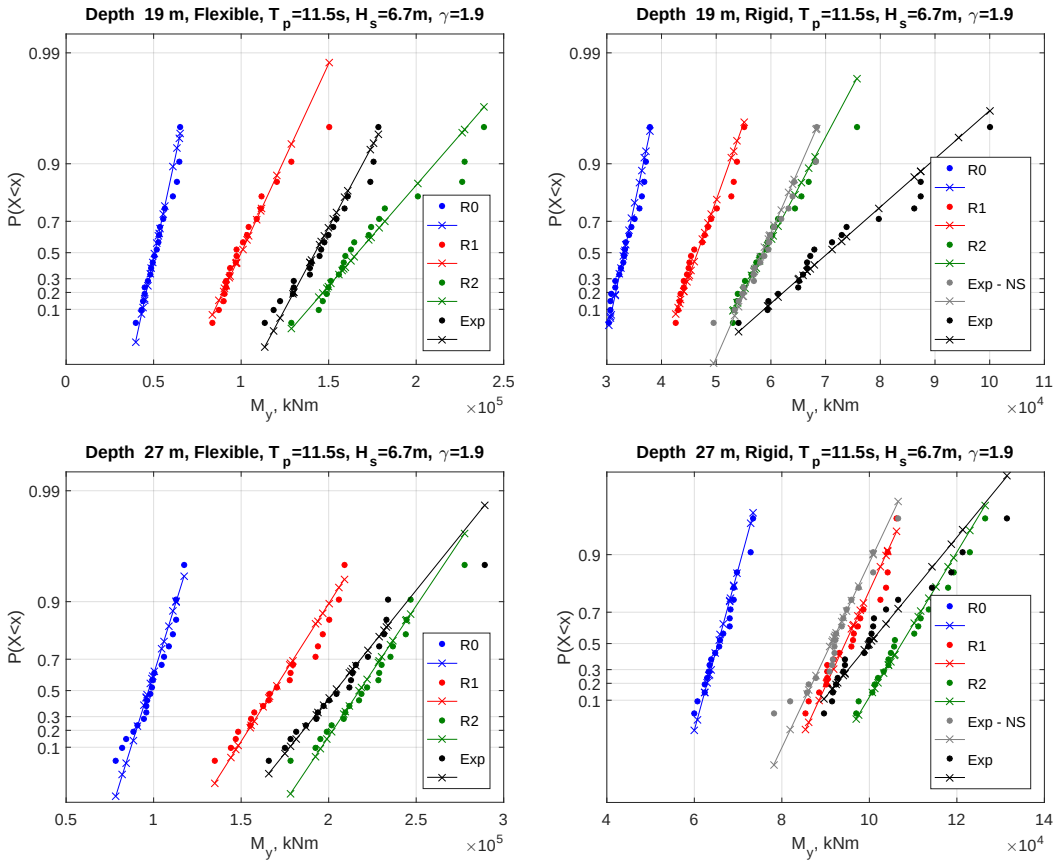

Figure 17: Gumbel distribution of maximum bending moment $H_s = 6.7$ m, $T_p = 11.5$ s, $\gamma = 1.9$, both water depths and models, all numerical models.

The results in Fig. 17 represent an example for one sea state; the 90th percentile bending moment at the

dynamometer is compared for each of the sea states, water depths, and structural models in Fig. 18. Considering the response of the flexible model, the 2nd order wave kinematics combined with the modified Morison's equation (R2) matched well for 27 m water depth, while the results were somewhat overestimated for the 19 m water depth. The overprediction was most severe for the sea states with shorter wave peak periods. Considering the good agreement in the R2 results and the non-slamming maxima for the rigid model, one explanation for the severe overestimation of the response of the flexible model in short sea states may be 2nd order diffraction effects. Although the magnitude of the loads was reasonably well estimated by the R2 model, the frequency content may be incorrect, that is, 2nd and 3rd order loads may be overestimated. For the flexible model, the R1 numerical model gave reasonable results (especially for the 19 m water depth) in the smallest sea states, but was found to be non-conservative for the highest sea states. Importantly, one may also note that correct predictions of maximum loads on the rigid model were not necessarily well correlated with accurate predictions of maximum responses of the flexible model.

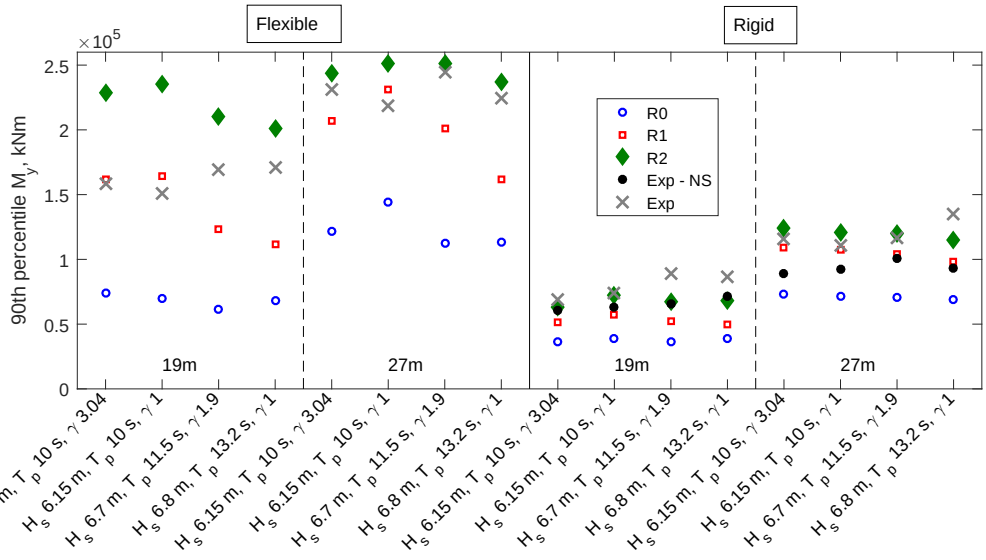

Figure 18: 90th percentile bending moment at the base of the spring (2.4 m below the mudline) from experimental and numerical results. Exp-NS results indicates the results in the absence of observed slamming effects due to breaking waves. All main tests are included.

Fig. 18 also shows that the maximum expected response of the flexible model in 27 m water depth corresponds to the sea state with a peak period (T_p=11.5 s) that is approximately 3 times the natural period of the model, while the maximum hydrodynamic loads on the rigid model (including slamming) were observed for the sea state with the highest H_s and longest waves (T_p=13.2 s). This was the wave condition for which the most wave breaking was observed. In 19 m water depth, the two highest sea states gave the highest hydrodynamic loads and the largest responses in the experiments, while the numerical simulations did not show the same trend.

4.3. Numerical sensitivity studies

The experimental setup was limited to one flexible configuration, that is, the structural natural frequency and damping level were not varied. In reality, the natural frequency of a monopile wind turbine may deviate from

the design value, and this natural frequency may in fact vary over the lifetime of the structure. Furthermore, in parked conditions, the damping is dictated by soil, structural, and hydrodynamic damping, and is typically quite low. Since both the underlying springing response and also the ringing response occur at the natural frequency, the damping level will have an effect on the response. In order to extend the applicability of the results from the present experimental and numerical campaign, sensitivity studies were carried out by considering 1) ± 10 % changes in natural frequency and 2) variations in the structural and wave radiation damping. Numerical studies were carried out for both the single-mode structure and a generic simplified fully-flexible monopile model. The first mode shape and the deflections of the single mode and the fully flexible model are shown in Fig. 19. The second mode shape of the fully-flexible model (not shown) is at 1.96 Hz.

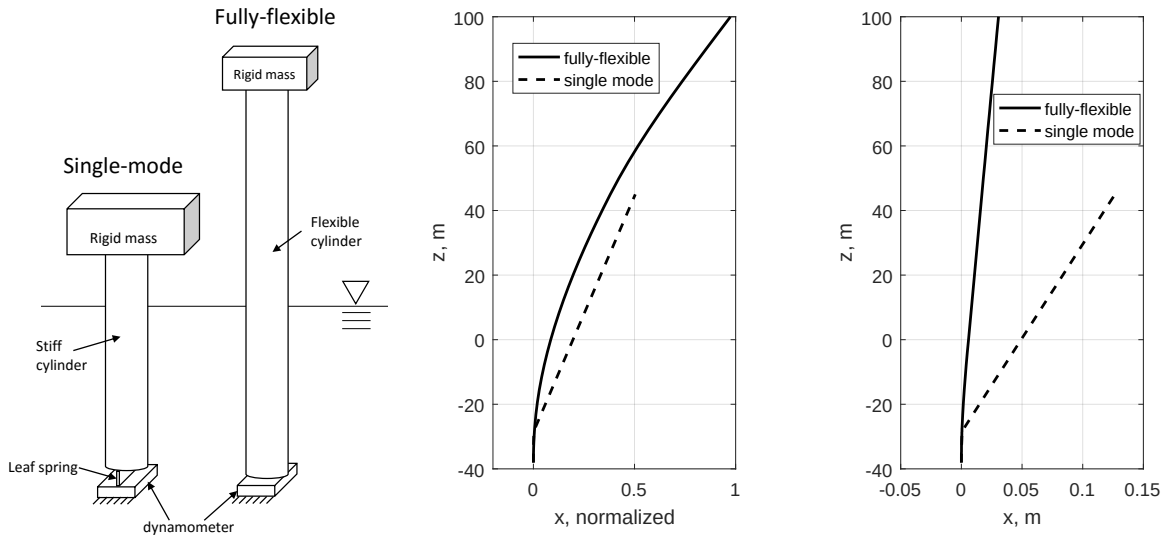

Figure 19: Comparisons of the model-of-the-model and fully flexible model. Schematic comparison (left, not to scale), first mode shape at 0.27 Hz (middle) and deflection due to a reference load at the waterline (right). 27 m water depth.

As shown, although the first natural frequency is in good agreement (0.27 Hz full scale for both models) and the fully-flexible model has a relatively linear mode shape along the wetted length, the displacement of the fully-flexible model in the wave zone is significantly smaller for the same reference load. For a given reference load at the waterline, the displacement of the "rotor" mass is also larger for the single-mode model compared to the fully-flexible model, despite the reduced height. As a result, the component of the overturning moment which is induced by the rotor mass can be expected to be larger for the single mode model than the fully-flexible model. Furthermore, the selected designs represent a limited number of combinations of stiffness and top mass. The contributions of the rotor mass to dynamic response depend on these design choices. As such, these comparisons should be regarded as illustrative.

4.3.1. Effect of natural frequency

In order to investigate the sensitivity to natural frequency, the stiffness in the numerical models was modified in order to obtain natural frequencies of 0.24 Hz and 0.29 Hz (±10 % vs initial). The stiffness was changed such that the mode shapes of the modified models were unchanged compared to the initial models. The same calibrated wave

time series from the experiments were used to calculate the 90th percentile bending moment responses, using the procedure described in the previous section. The results using the R2 model are shown in Fig. 20. The damping in these models is taken to only include the default structural damping and the viscous damping (no wave radiation damping).

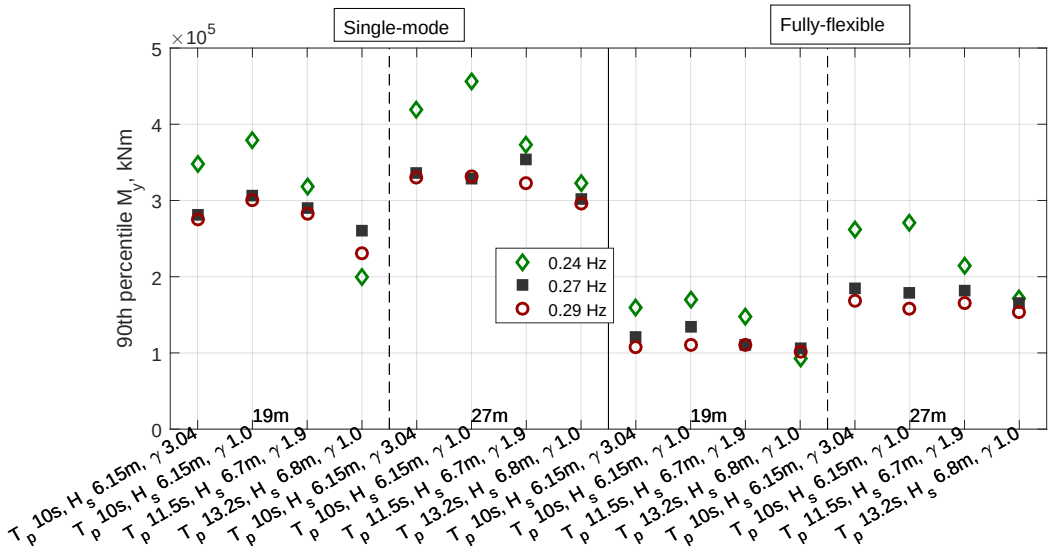

Figure 20: Sensitivity to natural frequency. 90th percentile bending moment at the base, R2 numerical model without wave radiation damping.

The magnitude of the response for the single mode and fully flexible models cannot be directly compared: the models were not designed to give equal bending moment responses, but to behave similarly. The comparison of results in Fig. 20 shows that the single mode model did indeed behave in a manner which is representative of the more realistic model. In general, the responses decreased for increasing natural frequency, that is, the stiffer structures had smaller responses. In particular, a decrease in the natural frequency gave a significant increase in the response for lower values of T_p. As the natural frequency decreases, there is an increase in first order wave loads at the structural natural frequency, and a decrease in the structural stiffness. The effect of the change in first order wave loads is especially noticeable for the broad-banded spectrum: as one moves from 0.27 Hz to 0.24 Hz, the theoretical value of the linear wave amplitude increases by 29 %. The corresponding increase in the first order wave load is smaller (around 5 %). However, the increase in first order wave loads and decrease in stiffness account for only part of the sensitivity to natural frequency: effects such as the nonlinear wave loads, phasing, and underlying springing response should also be investigated more closely in future work.

4.3.2. Effect of damping

In order to test the sensitivity to damping, three additional models were considered. In the first two models, the structural damping was increased by a factor of two and by a factor of 5. The third damping variation included the wave radiation damping via depth-dependent coefficients (see Section 3). The same damping coefficients were applied in both the single-mode and fully-flexible model with 0.27 Hz natural frequency. The wave radiation damping was only used in the final damping variation.

Fig. 21 shows the 90th percentile bending moment for the single-mode model and the fully flexible model. Increased damping reduced the extreme bending moment. It is important to note, however, that a careful examination of the time series showed that this conclusion only held for the overall response, not for individual events (where phasing may be important). The damping affected the ringing response implicitly by modifying the underlying springing response. Wave radiation damping had a significant effect on the single-mode model, especially at 27 m water depth, but can be seen to be less important for the fully flexible model, which had smaller displacements below the still water line. The effect of various damping levels was consistent within each water depth and structural model.

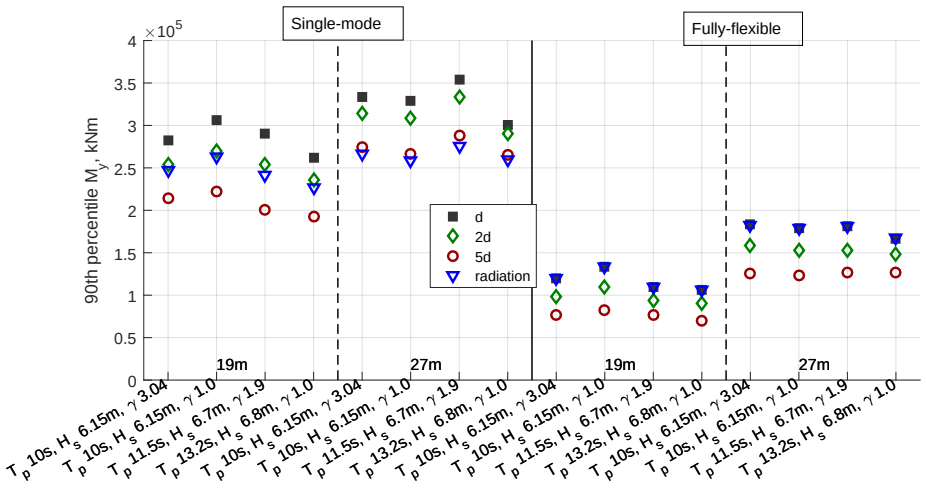

Figure 21: Sensitivity to damping. 90th percentile bending moment at the base, R2 numerical model.

For the single-mode model, doubling the damping (from approximately 1 % to approximately 2 % of critical) resulted in a reduction of 5-15 % in the 90th percentile bending moment. Multiplying the damping by a factor of five gave a corresponding 15-30 % reduction in the 90th percentile bending moment. The addition of the wave radiation damping coefficients was similar to doubling the structural damping for the 19 m water depth, while the effect was similar to multiplying the structural damping by a factor of five for the 27 m depth.

For the fully flexible model, doubling the damping from approximately 1 % to approximately 2 % critical resulted in a reduction of 15-20 % in the 90th percentile bending moment. The reduction was larger for the 19 m water depth. Multiplying the damping by a factor of five gave a corresponding 25-40 % decrease. The effect of the radiation damping coefficients was minimal for the fully flexible model: the velocity of the submerged sections was relatively small. Based on the sensitivity study results, uncertainties in the damping level should be considered when evaluating the ULS response to wave loads on monopile wind turbines.

5. Conclusions

The increasingly large diameter of monopile support structures for offshore wind turbines calls for greater attention to ULS wave loads and responses. Due to the typical natural periods of monopile wind turbines, nonlinear wave forcing may excite a transient resonant response, known as ringing. In the present experimental and numerical

studies, significant dynamic amplification of steep wave loads was seen in the flexible single degree-of-freedom model.

The experiments were set up carefully, and possible error sources were considered and mitigated where possible. The results were found to be highly repeatable. Automation in the experimental setup enabled a study of the stochastic variation in ringing-type responses, and corresponding numerical simulations were carried out for each combination of water depth, wave seed, and physical model. The numerical simulations employed a modified form of Morison's equation with 2nd order wave kinematics including convection terms and an additional linear damping term to account for radiation damping.

The extreme value of the bending moment at the base of the structure was evaluated experimentally and numerically. Stochastic variation in the 3-hour maximum value was significant (with a coefficient of variation up to 12 % for the flexible model and up to 23 % for the rigid model). Reasonable agreement between numerical and experimental extreme value analyses was seen for the flexible model, but slamming loads were important for the rigid model (and were not modelled numerically). The slope of the extreme value distribution was affected by slamming loads for the rigid model, but not for the flexible model. The modified Morison's equation with 2nd order wave kinematics overpredicted the (continuous, underlying) springing responses of the flexible model, but gave reasonable predictions of the extreme ringing responses in severe events. Overpredition of the extreme responses was seen for short waves ($T_p = 10$ s), especially in the shallower depth.

Sensitivity studies showed that the single degree-of-freedom model behaved similarly to a fully flexible model when considering changes in natural frequency and damping, except that the single degree-of-freedom model was more sensitive to wave radiation damping. In general, the responses were found to decrease for increasing natural frequency, i.e. the stiffer structures had smaller responses. As the damping increased, the maximum response decreased. Doubling the damping resulted in a response reduction of 5-20 %.

The present results suggest that the numerical model can be successfully applied to some relevant conditions for monopiles in finite water depth. Its applicability should still be carefully examined, however, for even shallower water - especially with respect to the validity range of the 2nd order wave model. Further study of the higher order loads including diffraction effects, numerical modelling of nonlinear irregular wave kinematics, and higher fidelity structural models should be considered in future work.

Acknowledgments

Statoil, Statkraft, and Masdar have graciously granted permission to present experimental and numerical results which were obtained at SINTEF Ocean. Dr. Madjid Karimirad and Sigrid Ringdalen Vatne of SINTEF Ocean contributed to the sensitivity studies. Dr. Reza Firoozkoohi of SINTEF Ocean contributed in discussions regarding the choice of the hydrodynamic coefficients C_a and C_d. Dr. Csaba Pákozdi of SINTEF Ocean contributed to the wave linearization.

References

[1] O. M. Faltinsen, J. N. Newman, T. Vinje, Nonlinear wave loads on a slender vertical cylinder, Journal of Fluid Mechanics 289 (1995) 179–198. arXiv:http://journals.cambridge.org/article_S0022112095001297,

doi:10.1017/S0022112095001297.

[2] J. N. Newman, Waves and nonlinear processes in hydrodynamics, Kluwer, 1996, Ch. Nonlinear scattering of long waves by a vertical cylinder, pp. 91–102.

[3] S. Malenica, B. Molin, Third-harmonic wave diffraction by a vertical cylinder, Journal of Fluid Mechanics 302 (1995) 203–229.

[4] J. Grue, G. Bjørshol, Ø. Strand, Higher harmonic wave exciting forces on a vertical cylinder, Tech. rep., Preprint Series, Matematisk Institutt Oslo (1993).

[5] R. C. T. Rainey, Slender-body expressions for the wave load on offshore structures, Proceedings: Mathematical and Physical Sciences 450 (1995) 391–416.

[6] Y. M. Scolan, B. Molin, G. Deleuil, D. Martigny, Experimental and numerical modelling of the high frequency resonant motion of a vertical cylinder in irregular waves, in: Proceedings of the 15th International Conference on Offshore Mechanics and Arctic Engineering (OMAE1996), Vol. I, 1996, pp. 389–396.

[7] C. T. Stansberg, Comparing ringing loads from experiments with cylinders of different diameters - an empirical study, in: 8th International Conference on the Behaviour of Off-Shore Structures (BOSS'97), 1997.

[8] J. Wienke, H. Oumeraci, Breaking wave impact force on a vertical and inclined slender pile - theoretical and large-scale model investigations, Coastal Engineering 52 (2005) 435–462.

[9] L. de Vos, P. Frigaard, J. de Rouck, Wave run-up on cylindrical and cone shaped foundations for offshore wind turbines, Coastal Engineering 54 (2007) 17–29.

[10] J. Zang, P. H. Taylor, G. Morgan, R. Stringer, J. Orszaghova, J. Grice, M. Tello, Steep wave and breaking wave impact on offshore wind turbine foundations - ringing re-visited, in: International Workshop on Water Waves and Floating Bodies (IWWWFB25), 2010.

[11] E. J. de Ridder, P. Aalberts, J. van den Berg, B. Buchner, J. Peeringa, The dynamic response of an offshore wind turbine with realistic flexibility to breaking wave impact, in: ASME 2011 30th International Conference on Ocean, Offshore and Arctic Engineering, no. OMAE2011-49563, 2011.

[12] A. W. Nielsen, F. Schlütter, J. V. T. Sørensen, H. Bredmose, Wave loads on a monopile in 3D waves, in: ASME 2012 31st International Conference on Ocean, Offshore and Arctic Engineering, no. OMAE2012-83533, 2013.

[13] H. Bredmose, M. Dixen, A. Ghadirian, T. Larsen, S. Schløer, S. Andersen, S. Wang, H. Bingham, O. Lindberg, E. Christensen, M. Vested, S. Carstensen, A. Engsig-Karup, O. Petersen, H. Hansen, J. Mariegaard, P. Taylor, T. Adcock, C. Obhrai, O. Gudmestad, N. Tarp-Johansen, C. Meyer, J. Krokstad, L. Suja-Thauvin, T. Hanson, DeRisk - accurate prediction of ULS wave loads. outlook and first results, Energy Procedia 94 (2016) 379 – 387, 13th Deep Sea Offshore Wind R&D Conference, EERA DeepWind'2016. doi:http://dx.doi.org/10.1016/j.egypro.2016.09.197.

[14] H. Bredmose, P. Slabiak, L. Sahlberg-Nielsen, F. Schlütter, Dynamic excitation of monopiles by steep and breaking waves. experimental and numerical study, in: 32nd International Conference on Ocean, Offshore and Arctic Engineering, no. OMAE2013-10948, 2013.

[15] B. T. Paulsen, H. Bredmose, H. B. Bingham, An efficient domain decomposition strategy for wave loads on surface piercing circular cylinders, Coastal Engineering 86 (2014) 57 – 76. doi:http://dx.doi.org/10.1016/j.coastaleng.2014.01.006.

[16] S. Schløer, H. Bredmose, H. B. Bingham, The influence of fully nonlinear wave forces on aero-hydro-elastic calculations of monopile wind turbines, Marine Structures 50 (2016) 162–188.

[17] B. T. Paulsen, H. Bredmose, H. B. Bingham, S. Schløer, Steep wave loads from irregular waves on an offshore wind turbine foundation: computation and experiment, in: 32nd International Conference on Ocean, Offshore and Arctic Engineering, no. OMAE2013-10727, 2013.

[18] G. K. Batchelor, An Introduction to Fluid Dynamics, Cambridge University Press, Cambridge, 1970.

[19] T. Kristiansen, O. M. Faltinsen, Ringing excitation wave loads on a vertical cylinder in finite water depth, Journal of Fluid Mechanics (under review).

[20] C. T. Stansberg, Characteristics of steep second-order random waves in finite and shallow water, in: Proceedings of the ASME 30th International Conference on Ocean, Offshore and Arctic Engineering OMAE2011, Rotterdam, The Netherlands, 2011.

[21] H. A. Schäffer, Second-order wavemaker theory for irregular waves, Ocean Engineering 23 (1996) 47–88.

[22] M. Tucker, P. Challenor, D. Carter, Numerical simulation of a random sea: a common error and its effect upon wave group statistics, Applied Ocean Research 6 (2) (1984) 118 – 122. doi:http://dx.doi.org/10.1016/0141-1187(84)90050-6.
URL http://www.sciencedirect.com/science/article/pii/0141118784900506

[23] E. Bouws, H. Günther, W. Rosenthal, C. L. Vincent, Similarity of the wind wave spectrum in finite depth water: 1. Spectral form, Journal of Geophysical Research: Oceans 90 (C1) (1985) 975–986. doi:10.1029/JC090iC01p00975.
URL http://dx.doi.org/10.1029/JC090iC01p00975

[24] O. M. Faltinsen, Ringing loads on a slender vertical cylinder of general cross- section, Journal of Engineering Mathematics 35 (1) (1999) 199–217. doi:10.1023/A:1004362827262.
URL http://dx.doi.org/10.1023/A:1004362827262

[25] Det Norske Veritas, Design of offshore wind turbine structures, Tech. Rep. DNV-OS-J101 (2007).

[26] T. Marthinsen, S. R. Winterstein, On the skewness of random surface waves, in: The Second International Offshore and Polar Engineering Conference, San Francisco, California, USA, 1992.

[27] C. T. Stansberg, O. T. Gudmestad, S. K. Haver, Kinematics under extreme waves, Journal of Offshore Mechanics and Arctic Engineering 130 (2) (2008) 021010. doi:10.1115/1.2904585.
URL http://dx.doi.org/10.1115/1.2904585

[28] J. Krokstad, C. Stansberg, A. Nestegård, T. Marthinsen, A new nonslender ringing load approach verified against experiments, Transactions of the ASME Journal of Offshore Mechanics and Arctic Engineering 120 (1) (1998) 20–29.

[29] L. Suja-Thauvin, J. R. Krokstad, E. E. Bachynski, E.-J. de Ridder, Experimental results of a multimode monopile offshore wind turbine foundation subjected to steep and breaking irregular waves, Ocean Engineering (under review).